JGR Earth Surface

RESEARCH ARTICLE
10.1029/2020JF006048

Large-Scale Scour in Response to Tidal Dominance in Estuaries

J. R. F. W. Leuven[1,2], D. van Keulen[1,3], J. H. Nienhuis[4], A. Canestrelli[5], and A. J. F. Hoitink[1]

[1]Department of Environmental Sciences, Hydrology and Quantitative Water Management Group, Wageningen University, Wageningen, The Netherlands, [2]Royal HaskoningDHV, Rivers & Coasts (Water), Nijmegen, The Netherlands, [3]Deltares, Delft, The Netherlands, [4]Faculty of Geosciences, Utrecht University, Utrecht, The Netherlands, [5]Department of Civil and Coastal Engineering, University of Florida, Gainesville, FL, USA

Key Points:

- Tidal funneling creates large-scale scours when channel convergence exceeds friction effects such that peak velocities are amplified
- A simple metric shows that large-scale scours appear in channels with large tidal amplitudes and short convergence lengths
- Estuary shape, fluvial, and tidal discharge predict scouring behavior now and under future changes, such as sea-level rise

Supporting Information:

Supporting Information may be found in the online version of this article.

Correspondence to:

J. R. F. W. Leuven,
jasper.leuven@wur.nl

Citation:

Leuven, J. R. F. W., van Keulen, D., Nienhuis, J. H., Canestrelli, A., & Hoitink, A. J. F. (2021). Large-scale scour in response to tidal dominance in estuaries. *Journal of Geophysical Research: Earth Surface*, *126*, e2020JF006048. https://doi.org/10.1029/2020JF006048

Received 22 DEC 2020
Accepted 3 MAY 2021

Abstract Channel beds in estuaries and deltas often exhibit a local depth maximum close to the river mouth. There are two known mechanisms of large-scale (i.e., >10 river widths along-channel) channel bed scours: width constriction and draw-down during river discharge extremes, both creating flow acceleration. Here, we study a potential third mechanism: tidal scour. We use a 1D-morphodynamic model to reproduce tidal dynamics and scours in estuaries that are in morphologic equilibrium. A morphologic equilibrium is reached when the net (seaward) sediment transport matches the upstream supply along the entire reach. The residual (river) current and river-tide interactions create seaward transport. Herein, river-tide interactions represent the seaward advection of tide-induced suspended sediment by the river flow. Tidal asymmetry typically creates landward transport. Scours form when tidal flow is amplified through funneling of tidal energy. Scours simultaneously reduce the residual (river) current and the river-tide interaction contribution to sediment transport, thereby maintaining morphologic equilibrium. When tidal influence is relatively large, and when channel convergence is strong, an equilibrium is only obtained with a scouring profile. We propose a predictor dependent on the width convergence, quantified as S_B, and on the ratio between the specific peak tidal discharge at the mouth and the specific river discharge at the landward boundary (q_{tide}/q_{river}). Scours develop if $(q_{tide}/q_{river})/S_B$ exceeds 0.3. Scour conditions were found to occur globally across a range of scales, which allows its prediction in estuaries under future changes.

Plain Language Summary Estuaries form the transitions from rivers to the ocean. The maximum depth of an estuary often occurs at the mouth. Occasionally, estuaries have their maximum depth further inland of the mouth. Such a depression in the bed-level profile often occurs over a distance much larger than the channel width. We call this "large-scale scour." So far, two explanations for large-scale scour exist, and in this article, we investigated a third mechanism that we term tide-induced scour. We show with simplified numerical models that there are two main factors that control whether tide-induced scours can form: (a) the planform shape of the channel and (b) the extent of tidal influence with respect to the river discharge. When the planform geometry is more strongly convergent in landward direction and/or when the tidal influence is relatively large compared to the fluvial influence, the potential for tide-induced scour is large. In this study, we present a predictor that allows to establish the tide-induced scour potential in estuaries worldwide. Understanding of tide-induced scour and the prediction tool help anticipating how estuaries will evolve in the future under changing climate, land use, and sea-level rise.

1. Introduction

Estuaries and deltaic channels are dynamic environments at the transition from the river to the ocean (Figure 1). These coastal channels are of special importance for mankind in terms of transport (de Vriend et al., 2011) and ecological value (Bouma et al., 2005). The surrounding land is often densely populated (Edmonds et al., 2020), with 21 of the world's 30 largest cities being located next to estuaries (Ashworth et al., 2015).

Channel dimensions are a result of interactions between river flow and tides (Bolla Pittaluga et al., 2015; Canestrelli, Lanzoni, & Fagherazzi, 2014; Friedrichs & Aubrey, 1988; Savenije, 2006). Recent efforts allowed for a better understanding of the causes of estuarine width, which enable to predict estuarine width and

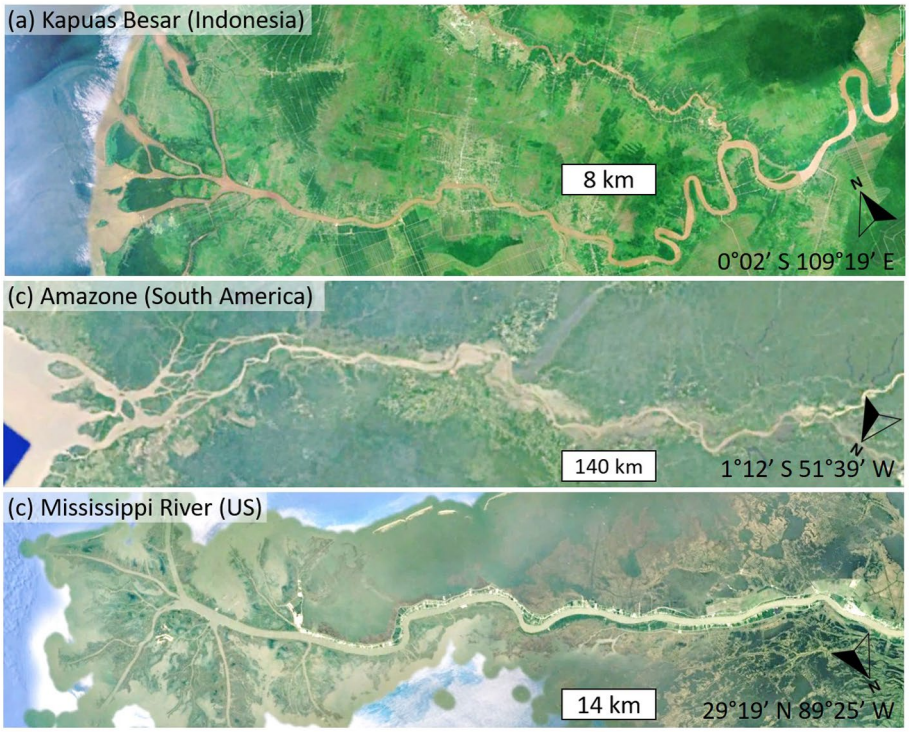

Figure 1. Large-scale bed degradation, also called scour, occurs in systems of different sizes and from all around the world. Three estuaries with observed scours are (a) the Kapuas Besar in Indonesia, (b) the Amazon River in South America, and (c) the Mississippi River in the United States. The corresponding bed-level profiles with scour are shown in Figure 2. Aerial photographs were obtained from Google Earth.

relate width to tidal influence (Leuven, van Maanen, et al., 2018; Nienhuis et al., 2018). Less is known yet about estuarine depth. Along-channel bathymetric data are sparse, because they are usually only collected for the engineered systems and rarely for the few systems that could still be regarded as pristine. Also, geological constraints including erosion resistant layers and banks cause that the scouring process we address is often masked by the complexity of real-world systems. However, understanding the natural evolution of estuarine channel beds is of importance because channel bed deepening can threaten bank stability, while channel shallowing can reduce navigability. Future changes in boundary conditions, such as sea-level rise or drought-induced discharge decrease, may affect hydrodynamics and thereby induce large-scale channel bed degradation (Du et al., 2018; Leuven et al., 2019) or channel infilling (Nienhuis et al., 2018). Here we investigate tidal and fluvial controls on estuarine channel depth and channel scours, defined here as large-scale (scour length >10 river widths in the along-channel direction) channel bed depressions.

Rivers maintain approximately constant along-channel width and depth under steady boundary conditions (Dunne & Jerolmack, 2020; Hey & Thorne, 1986; Leopold & Maddock, 1953; Mikhailov, 1970). Approaching the coast, tides can lead to an expansion of the channel width, resulting in a trumpet or funneled shape from seaward increase in discharge and tidal volume (Langbein, 1963; Savenije, 2006). For some estuaries, including headless tidal channels (D'Alpaos et al., 2017; Lanzoni & Seminara, 2002), channel depth also increases seawards. Other estuaries, however, show sediment deposition and seaward channel shallowing from flow expansion and deceleration (Dalrymple et al., 2003; Hart, 1995). In between these end-members, there are estuaries and deltas with channel depths that are neither monotonically increasing or decreasing, but have their greatest depth just landward of their mouth (Figure 2). This includes actively prograding deltaic channels where mouth bars form (Canestrelli, Nardin, et al., 2014; Edmonds & Slingerland, 2007) and also estuaries in equilibrium (Guo et al., 2015b; Lamb et al., 2012; Lane, 1957; Toffolon & Lanzoni, 2010). Equilibrium here refers to a morphodynamic balance in which the width-average bed level remains constant in time, and the total sediment load equals the upstream sediment input.

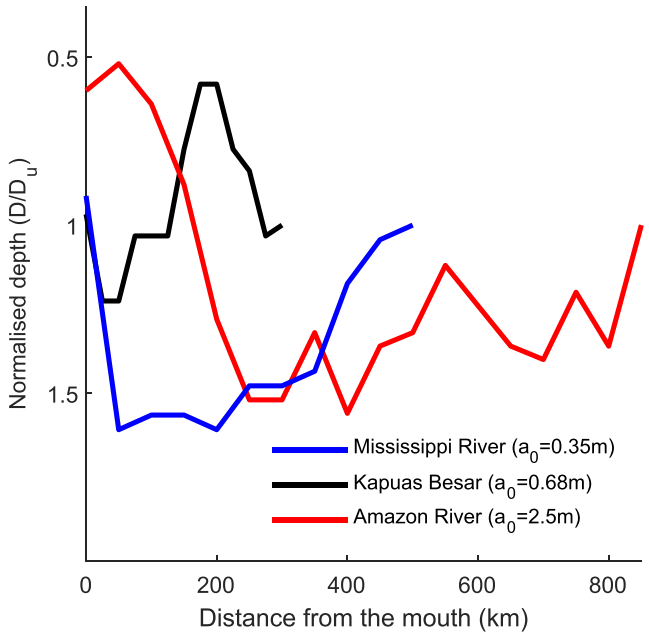

Figure 2. Width-averaged depths along river deltas and estuaries and associated tidal amplitudes (a_0) at the mouth. The depth (D) is normalized by the upstream depth (D_u). L_t corresponds to the total length of the system, which is 300 km for the Kapuas, 850 km for the Amazon, and 500 km for the Mississippi. These lengths roughly correspond to the tidal intrusion lengths during low flow conditions or the upstream extent of the observed scour in these estuaries. Data are interpreted from Lamb et al. (2012), Kästner et al. (2017), Venditti et al. (2015), Gallo and Vinzon (2005).

Multiple studies have been dedicated to long-term channel bed development to obtain an understanding of the observed depths along estuaries and deltas (Bolla Pittaluga et al., 2015; Braat et al., 2017; Canestrelli, Lanzoni, & Fagherazzi, 2014; Tambroni et al., 2005; Todeschini et al., 2008) and potential causes for large-scale channel bed degradation. These studies highlight three mechanisms known for large-scale channel bed depressions that are also known as "scours." The first mechanism is topographic forcing by human or geological constraints (Leuven, de Haas, et al., 2018). Width constrictions create flow convergence and cause local scour. The second mechanism is induced by river floods (Lamb et al., 2012; Lane, 1957). A draw-down of the water profile that establishes during floods causes spatial flow accelerations that lead to scouring.

The third mechanism is tide-induced (Bolla Pittaluga et al., 2015; Guo et al., 2015b). Interactions between tides, river flow, and channel convergence in landward direction lead to funneling of the tide, which causes scour. However, the conditions under which scours form are not yet well understood. For example, while Bolla Pittaluga et al. (2015) found minima in the bed-level profile at the estuary mouth, they did not find a scour profile in which the bed profile shows a minimum landward of the mouth. In contrast, Guo et al. (2015b) obtained a scour profile for a converging channel. They addressed the role of river discharge on the sediment supply and reinforcement of the ebb-directed residual transport. While the first two are relatively well-known mechanisms, the conditions under which tscours form are quite under-explored.

Here we study the effect of tidal dominance on the equilibrium channel bed in estuaries and delta branches to find under which conditions large-scale tidal scours occur. We hypothesize that a certain degree of tidal influence in combination with the funneling of estuaries can result in large-scale channel bed scour. To test this, we use a 1D-morphodynamic model that reproduces the hydrodynamic and morphological evolution of an estuary (Bolla Pittaluga et al., 2015; Canestrelli, Lanzoni, & Fagherazzi, 2014). First, we investigate a set of idealized cases for converging channels on three spatial scales. Channel dimensions are chosen consistent with a small (250 m^3/s), medium (500 m^3/s), and large (1,000 m^3/s) river discharge. For each scale, we varied the degree of tidal influence by increasing the tidal amplitude. Subsequently, we show that the model projects a large-scale channel bed scour in the Amazon River. This is roughly consistent with observations and indicates that tides are the likely mechanism for scour formation in the largest river on Earth.

2. Methods and Materials

2.1. Model Description

We used FV-SED (Canestrelli, Lanzoni, & Fagherazzi, 2014) to compute the bottom development along tidally influenced channels. FV-SED is a 1D-hydro-morphodynamic model, which has been proven suitable to reproduce the morphological development of channel beds (Bolla Pittaluga et al., 2015; Canestrelli, Lanzoni, & Fagherazzi, 2014).

The cross section in FV-SED is schematized as a rectangle in which the bottom depth can change in time as a result of morphodynamic development. The channel can have a variable along-channel width profile ($B(x)$). Hydrodynamic conditions and morphological changes were modeled with cross-sectional averaged equations for mass (Equation 1) and momentum (Equation 2), and the one-dimensional Exner equation for bed evolution (Equation 4). In the momentum balance, possible baroclinic- and Coriolis-induced effects were neglected. The equations for mass and momentum read:

$$\frac{\partial B(H - Z_b)}{\partial t} + \frac{\partial Q}{\partial x} = 0, \tag{1}$$

$$\frac{\partial Q}{\partial t} + \frac{\partial}{\partial x}\left(\frac{Q^2}{B(H-Z_b)} + \frac{1}{2}gB(H-Z_b)^2\right) = \frac{1}{2}g(H-Z_b)^2\frac{\partial B}{\partial x} - gB(H-Z_b)\frac{\partial Z_b}{\partial x} - gBR_hS_f, \quad (2)$$

in which Q denotes the discharge, B the channel width, H the water level elevation, Z_b the bottom elevation, g the gravitational acceleration, R_h the hydraulic radius, and S_f is friction slope. The latter is given by:

$$S_f = \frac{Q^2}{B^2D^2C^2\sqrt{R_h}}, \quad (3)$$

in which D is the water depth and C is the Chézy roughness coefficient. The bed evolution is calculated according to the Exner equation:

$$\frac{\partial(1-p)BZ_b}{\partial t} + \frac{\partial Q_S}{\partial x} = 0, \quad (4)$$

in which p is the bed porosity and Q_S the total sediment load. The sediment load per unit width is given by the Engelund and Hansen (1967) equation:

$$q_s = \frac{0.05u^5}{\sqrt{g}\Delta^2C^3D_{50}}, \quad (5)$$

in which u is the depth-averaged flow velocity, D_{50} is the average sediment diameter, and Δ is the immersed relative density. The total sediment load (Q_s) is obtained by multiplying the sediment load per unit width (q_s) by the channel width (B).

The estuary planform was fixed during simulations, which means that we assume that channel banks are nonerodible. Subsequently, the model was used to determine the equilibrium bed configuration for the prescribed initial and boundary conditions. This is a common approach in morphodynamic studies on tidal channels (Lanzoni & Seminara, 2002; Seminara et al., 2010; Todeschini et al., 2008; Toffolon & Lanzoni, 2010) and estuaries (Bolla Pittaluga et al., 2015; Canestrelli, Lanzoni, & Fagherazzi, 2014).

We used a morphological acceleration factor (MF) of 200 to accelerate the channel bed development (Roelvink, 2006). The morphological factor scales the morphological evolution with a time factor. The assumption behind this technique is that the timescales that characterize flow variations are much smaller than the morphological changes that take place. Tests with a value for MF of 1 and 200 showed that MF = 200 reproduced the bed levels obtained with a MF = 1.

The input variables of the model are: mean discharge (Q_b), bankfull discharge (Q_{bf}), tidal amplitude at the mouth (a_0), grain size (D_{50}), and simulation duration (t). In addition, the following constants were used: critical Shields number ($\Theta = 0.145$, which corresponds to a typical value for the chosen grain size), the Chézy roughness coefficient ($C = 55\ \mathrm{m}^{0.5}/\mathrm{s}$, typical for medium sized estuaries such as the Western Scheldt and Thames [Kleinhans et al., 2017]), tidal period ($T = 12.42$ h), immersed relative density ($\Delta = 1.65$, typical for sand), kinematic viscosity of water ($\nu = 1.0 \times 10^{-6}$), morphological acceleration factor (MF = 200) and gravity acceleration ($g = 9.81\ \mathrm{m/s}^2$).

The model does not consider cohesive sediment dynamics. In estuaries with mud, cohesion likely affects the scouring potential. Resistant mud deposits may limit vertical and lateral erosion. However, this is a topic that requires further exploration and was therefore not included in this study.

The results are independent of the model domain length, as long as the model domain is longer than the length over which there is tidal influence (Bolla Pittaluga et al., 2015), which we confirmed with a sensitivity analysis for model length. Therefore, we choose our domain length such that it captures the tidally influenced reach. Scenarios with a wider and deeper river or with a larger tidal range require a longer model domain, since they both favor an upstream lengthening of the tidally influenced reach.

Table 1
Initial Conditions and Boundary Conditions for All Model Runs

Size	Q_b (m^3/s)	Q_{bf} (m^3/s)	B_u (m)	B_0 (m)	D_u (m)	S_0 (m/m)	L_B (km)	a_0 (m)	Q_s (m^3/s)
Small estuary, sensitivity to tide	250	1,000	184	734	4.21	0.00011	15	1...3.5	0.017
Medium estuary, sensitivity to tide	500	2,000	292	1,168	5.10	0.00008	24	1...3.5	0.025
Large estuary, sensitivity to tide	1,000	4,000	464	1,856	6.17	0.00006	38	1...3.5	0.038
Medium estuary, sensitivity to convergence	500	2,000	292	1,168	5.10	0.00008	2...47	1	0.025
Medium estuary, sensitivity to convergence	500	2,000	292	1,168	5.10	0.00008	2...47	1.5	0.025
Medium estuary, sensitivity to convergence	500	2,000	292	1,168	5.10	0.00008	2...47	2	0.025
Medium estuary, sensitivity to sediment supply	500	2,000	292	1,168	5.10	0.00008	24	2.25	0.010...0.055
Small estuary, sensitivity to discharge and sed supply	2,50...1,000	1,000	184	734	4.21	0.00011	15	2.5	0.020...0.170
Medium estuary, sensitivity to D50 (0.10.4 mm)	500	2,000	292	1,168	5.10	0.00008	24	2.25	0.025
Medium estuary, sensitivity to Chézy (4,060 $m^{0.5}/s$)	500	2,000	292	1,168	5.10	0.00008	24	2.25	0.025
Amazon river (run 11 & 17)	169,000	230,000	4,220	96,250	18.9	0.00001	146	2.5	6.5

Note. For each size (small, medium and large), the tidal amplitude at the seaward boundary was systematically varied between 1 and 3.5 m to study the effect of tidal amplitude on the occurrence of large-scale channel bed scour.

Our scenarios extend the scenarios studied in Bolla Pittaluga et al. (2015), which did not show the formation of scours or depressions in the bed level. Bolla Pittaluga et al. (2015) modeled bankfull conditions for both flow and sediment supply. The resulting conditions were strongly river-dominated. Here, we used bankfull conditions to determine channel dimensions and yearly average conditions to determine flow and sediment supply. Bankfull conditions determine fluvial bed characteristics, but this scaling does not extend into the estuary. Therefore, we compare annual average fluvial conditions against annual average tidal conditions. A minor difference compared to the setup in Bolla Pittaluga et al. (2015) is that we used the Chézy coefficient instead of the Gauckler-Strickler friction coefficient.

2.2. Set-Up for Idealized Scenarios

To study the effect of tidal amplitude on the occurrence of large-scale bed scour, a set of idealized model scenarios was considered (Table 1). Tidal amplitude at the seaward boundary was systematically varied. To do so, we modeled a small ($Q_b = 250$ m^3/s), medium ($Q_b = 500$ m^3/s), and large ($Q_b = 1{,}000$ m^3/s) channel, adopting a value for D_{50} of 0.1 mm.

Channel dimensions at the upstream boundary were estimated from discharge with existing hydraulic geometry relations for bankfull discharge (Wilkerson & Parker, 2011). For simplicity, bankfull discharge (Q_{bf}) was assumed to be four times the mean discharge (Q_b) in idealized models:

$$Q_{bf} = 4Q_b. \tag{6}$$

Using Wilkerson and Parker (2011), the upstream channel width was given by:

$$B_u = 0.004\left(\frac{\sqrt{\Delta}}{\nu}\right)^{0.49} {Q_{bf}}^{0.67} g^{-0.09} {D_{50}}^{0.07}. \tag{7}$$

The next step was to estimate the channel planform in the seaward part of the domain. River mouths and estuaries are generally assumed to have an upstream-converging (also called trumpet or funnel) shape. The converging shape relates to the seaward increase in discharge or tidal volume (Langbein, 1963; Savenije, 2006; Townend, 2012). Even when width variations in natural estuaries are irregular, deviations from the converging shape can often be ascribed to the presence of intertidal bars (Leuven, Braat, et al., 2018). Many studies have attempted to find a relation between the degree of landward convergence and hydrodynamic forcings, such as tidal amplitude (Davies & Woodroffe, 2010; Dronkers, 2017; Savenije, 2006). While convergence was thought to typically scale with tidal range, recent data suggest that the correlation between

upstream (river) channel width and convergence length is stronger (Leuven, van Maanen, et al., 2018). Therefore, here we adopt an empirical relation to set the convergence length and mouth width in our model, based on data from 68 fluvial-tidal transition zones worldwide (Leuven, van Maanen, et al., 2018). For simplicity, we assume that the width at the mouth (B_0) is four times the width of the upstream river (B_u). The effect of estuary planform shape on channel bed profiles are described in the results. Convergence length (L_B) is estimated based on empirical relations (Leuven, van Maanen, et al., 2018) as:

$$L_B = 81 B_u. \tag{8}$$

The along-channel width profile is given by:

$$B = B_u + (B_0 - B_u)\exp\left(-\frac{x}{L_B}\right). \tag{9}$$

This approach resulted in estuary dimensions that fall within the range of natural systems (Nienhuis et al., 2018). Only for the largest tidal amplitudes ($a_0 > 3.0$ m), the mouth width used was smaller than expected for a natural system, where a large tidal prism in nature might widen the mouth. Nevertheless, we chose to vary only tidal amplitude and keep mouth width constant, to isolate the effect of tidal amplitude variations.

The initial bed slope and initial channel depth were estimated with the Wilkerson and Parker (2011) upstream hydraulic geometry relations, given by:

$$S_0 = 19\left(\frac{\sqrt{\Delta}}{\nu}\right)^{-0.20} g^{0.10} Q_{bf}{}^{-0.39} D_{50}{}^{0.69}, \tag{10}$$

and

$$D_u = 23\frac{\sqrt{R}}{\nu}^{-0.31} g^{-0.29} Q_{bf}{}^{0.28} D_{50}{}^{-0.16}. \tag{11}$$

The initial bed slope and channel depth only affect the time to reach equilibrium without altering the final result, as already found in previous studies (Bolla Pittaluga et al., 2015; Canestrelli, Lanzoni, & Fagherazzi, 2014).

The sediment load (Q_{Su}) at the upstream boundary was calculated with Engelund and Hansen (1967) from the average discharge (Q_b) and channel width (B_u) with:

$$Q_{Su} = 0.05 u^5 \frac{B_u}{\sqrt{g}\Delta^2 C^3 D_{50}}, \tag{12}$$

in which the depth-averaged flow velocity, u, is calculated as:

$$u = \left(C\sqrt{\frac{Q_{bf}}{B_u} S_0}\right)^{2/3}. \tag{13}$$

This approach assumes that the bankfull conditions set the size and shape of a river channel, as supported by the empirical data provided by Wilkerson and Parker (2011) and Kleinhans and van den Berg (2011). Application of bankfull conditions to other environments, such as alluvial basins, requires the use of an intermittency factor (Paola et al., 1992). However, application of an intermittency factor only works when bankfull discharge is the dominant formative process. In case of estuaries, typically, the semidiurnal tide is the dominant forcing agent. Therefore, we ignore seasonally variable discharge and assume that the yearly average sediment supply from upstream is responsible for the sediment delivery to the estuary. We based the use of a constant sediment discharge on Guo et al. (2015a). In that paper, it was shown that the long-term morphodynamic evolution of the estuary does not depend on the shape of the seasonally varying discharge, but only on the total volume of sediment entering the upstream riverine boundary over 1 year.

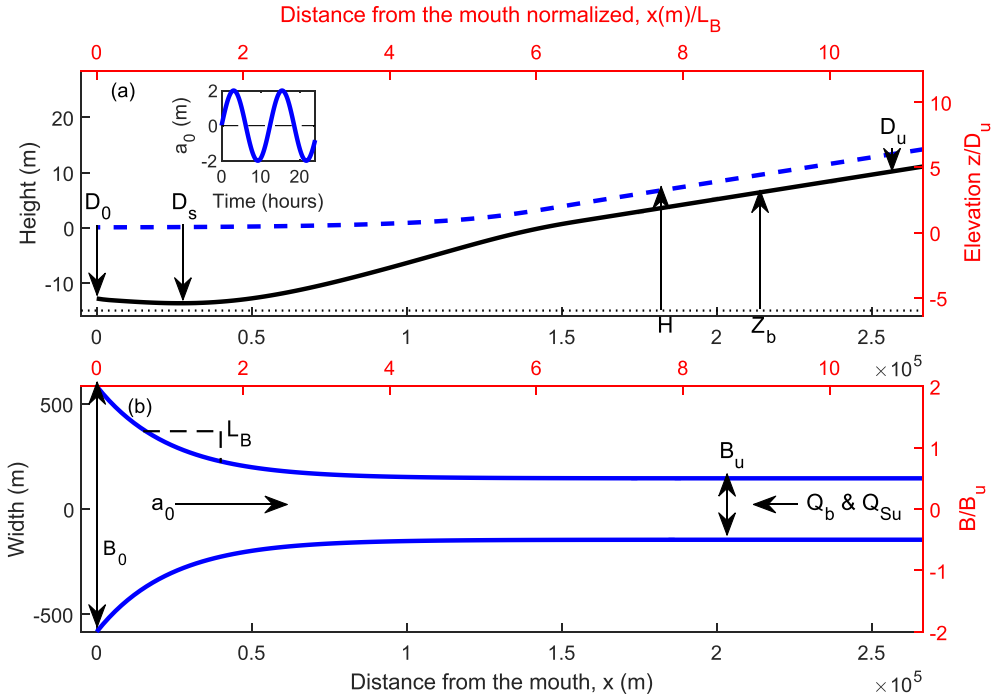

Figure 3. Example of model set-up. (a) Side-view of the investigated domain and used notations. The inset gives an example of the water level variations at the mouth. (b) Plan-view of the investigated domain and used notations. In both sketches, the *x*-axes indicate both the Cartesian distance from the mouth as the distance normalized by the convergence length (L_B). H indicates the water level elevation, Z_b the bed elevation, D_u the upstream river depth, B_u upstream channel width, B_0 mouth width, Q_b mean river discharge, Q_{su} sediment load as input at the upstream boundary, and a_0 the tidal amplitude at the mouth.

The domain length was set to 800 km for the idealized scenarios, such that both small and large systems would easily fit within the model domain under both small and large tidal ranges. Using a smaller domain length would result in boundary effects at the upstream boundary for the largest systems and systems with the largest tidal ranges. For all simulations, the number of along-channel grid cells was equal to 400, such that the grid cell size was 2 km.

The resulting set of initial and boundary conditions for the idealized scenarios is given in Table 1. An example of the initial conditions and model set-up is given in Figure 3. A sensitivity analysis focused on input parameters and constants was performed for the medium-sized system with a tidal amplitude of 2.25 m. We tested the sensitivity of the results to choices for the Chézy roughness coefficient, sediment supply, discharge and the value of D_{50}. An assessment of the sensitivity to system size and tidal amplitude is part of the main results of this study. Moreover, the model used has been used and tested for sensitivity before (Bolla Pittaluga et al., 2015; Canestrelli, Lanzoni, & Fagherazzi, 2014).

2.3. Set-Up for Scenarios Based on the Amazon River

In addition to the previous set of idealized scenarios, a set of scenarios was based on the properties of the Amazon River (Table 1). Tidal amplitude at the mouth was based on values reported by Gallo and Vinzon (2005) and Kosuth et al. (2009). An estimation of the average and bankfull discharge was made based on data in Kosuth et al. (2009). Grain size was set to 0.1 mm, following Nordin et al. (1980).

We used a sediment load at the upstream boundary of 6.5 m^3/s to ensure bed levels fall within the range reported by Gallo and Vinzon (2005). Other estimates of 7.2–15.6 m^3/s (Latrubesse et al., 2017), 11.7–14.3 m^3/s (Nienhuis et al., 2020), 3.0–5.0 m^3/s (based on Equation 12) are within the same order of magnitude.

The along-channel width profile was measured on Google Earth. The summed widths of the branches was used in the mouth area (Canestrelli, Lanzoni, & Fagherazzi, 2014). Additionally, an idealized width profile was used to exclude the effects of topographic forcing. Both cases are reported in this study.

2.4. Data Processing and Data Reduction

Definitions used to describe the planform shape of the channel and characteristics of the bed level are given in Figure 3. To characterize bed-level degradation, that is, scour, we compared the maximum water depth (D_s) with the depth at the mouth (D_0) and upstream river (D_u) (Figure 3). For depth calculations, the tidally averaged water level was used. The bed-level profile was classified as a scour profile when the maximum water depth (D_s) was larger than both the mouth depth (D_0) and the upstream river depth (D_u). In that case, a shallower zone occurs at the mouth. The cases in which the maximum depth correspond with the depth at the mouth were also recorded, but were not classified as scours.

Other definitions used in this study are the tidal dominance length and the shape factor. The shape factor (S_B) is calculated as the convergence length, that is, the distance over which the channel width converges with a factor $e \approx 2.7$, divided by mouth width minus river width ($S_B = L_B/(B_0 - B_u)$). The shape factor gives a dimensionless degree of convergence, thus independent of estuary size (Davies & Woodroffe, 2010). Lower values of S_B indicate stronger convergence.

The term horizontal tide refers to flow velocities, whereas the vertical tide represents the water level variation. The horizontal tide was analyzed by decomposition of the velocity signals:

$$u(t) = u_r + \sum_{i=2,4,\ldots}^{8} U_i \cos(\omega_i t + \phi_i), \tag{14}$$

in which u_r is the residual flow, U_2 is the current amplitude of the semi diurnal tide (M_2) and U_4 is the current amplitude of the first even harmonic over tide (M_4) and so on. ω_i are the angular frequencies and ϕ_i are the phases of the tidal constituents. The residual flow is the sum of the Stokes drift and the river induced current, so $u_r = u_{\text{Stokes}} + u_{\text{riv}}$. We can calculate the contribution by Stokes drift, because u_r can be computed from the model output as the integration of $u(t)$ over a tidal cycle divided by the tidal period and the river induced current can be calculated as $u_{\text{riv}} = Q_b / (B(x)\overline{D(x)})$, in which $\overline{D(x)}$ is the tidally averaged depth. The Stokes drift is the result of phase differences between the horizontal and vertical tide (Buschman et al., 2010; Sassi et al., 2011).

The majority of the energy is transferred from the M_2 to the M_4 tide. Energy is also transferred to the M_6 and M_8 tide, but they are less important than the M_4-component. Nevertheless, they were also included in the performed harmonic analysis for the decomposition of the tidal signal. We will show the decomposition of intertidal velocity fluctuation in the results solely in terms of U_2, U_4 and the phase difference between U_2 and U_4. All higher harmonics were including in calculations of the sediment balance.

The tidal dominance length (ℓ) is the distance over which the sediment transport is tide-dominated. The tidal dominance length is calculated as the distance from the mouth to the point where the sediment load transported by residual current (Q_{Sr}) divided by the sediment input at the boundary (Q_{Su}) equals 0.5. The residual current (u_r) is the tidally averaged integration of the velocity signal.

The total sediment load ($Q_{S,\text{tot}}$) can be decomposed into contributions by the river discharge only (Q_{Sr}), by the interaction of river discharge with the tide (Q_{Srt}), and by tidal asymmetry (Q_{St}) (Hoitink et al., 2017):

$$\left\langle Q_{S,tot} \right\rangle = \frac{1}{T}\int_0^T au^5 dt = Q_{Sr} + Q_{Srt} + Q_{St}. \tag{15}$$

The interaction term can be interpreted as advection of tide-induced resuspended sediment by the river flow. The total sediment load (i.e., the sum of Q_{Sr}, Q_{Srt}, and Q_{St}) equals the upstream sediment input at the boundary Q_{Su} when the system is in equilibrium. The sediment load transported by the residual current (Q_{Sr}) is given by:

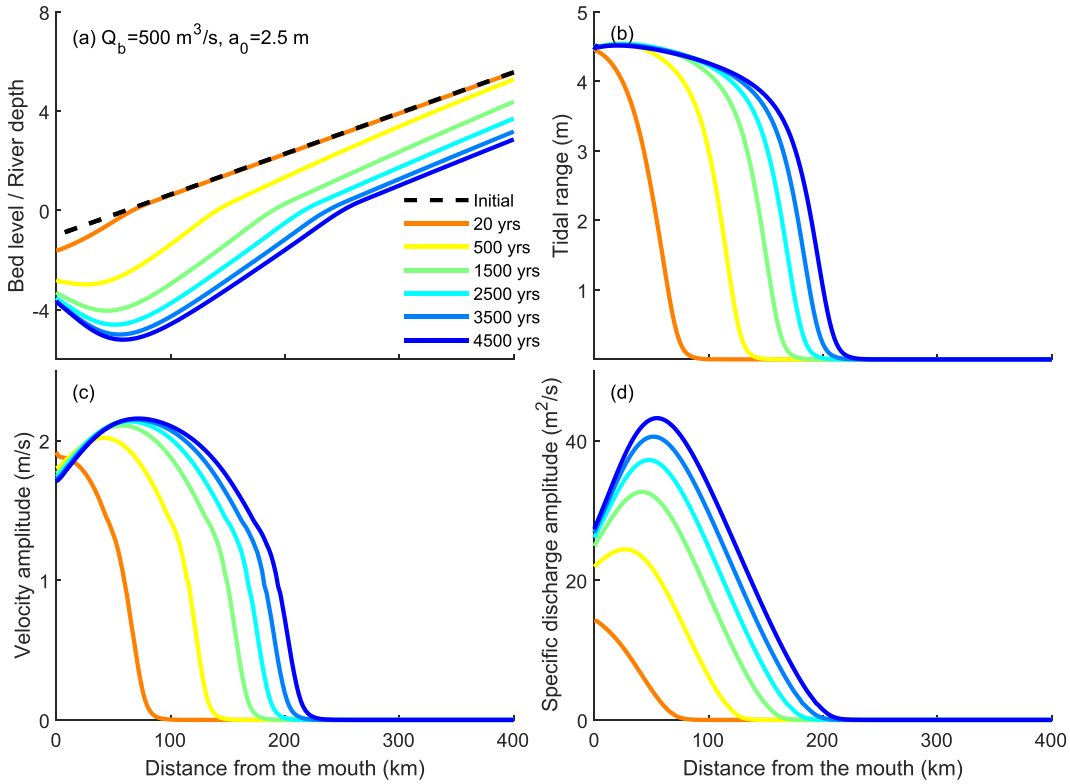

Figure 4. Resulting bottom profile (a), tidal range (b), velocity amplitude (c), and amplitude of specific discharge (d) at different stages in time for a model with a tidal amplitude of 2.5 m. From about 4,500 years, the tidally averaged sediment flux approximates to the upstream sediment load in the entire domain and the model reaches equilibrium.

$$Q_{Sr} = a u_r^{\,5} \tag{16}$$

The sediment load transported by the interaction of the residual current and tidal current (Q_{Srt}) reads:

$$Q_{Srt} = 5 a u_r^{\,3} (U_2^{\,2} + U_4^{\,2}) + \frac{15}{8} a u_r (U_2^{\,4} + U_4^{\,4}) + \ldots, \tag{17}$$

where small contributions from U_6 and U_8 have been omitted for readability. In the computations, the complete equation has been used. The sediment load transported by tidally induced asymmetry (Q_{St}) is given by:

$$Q_{St} = \frac{5}{4} a U_2 U_4^{\,4} cos(2\phi_2 - \phi_4) + \ldots, \tag{18}$$

Again, contributions from U6 and U8 have been omitted for readability.

3. Results

In the results below, the resulting equilibrium bed-level profile is considered as a key output. To assess this, we first checked how long it takes for the model to reach a morphodynamic equilibrium. On average, equilibrium is reached within roughly 4,500 years (Figure 4). Scenarios with a lower tidal amplitude reach equilibrium even sooner, while scenarios with a larger tidal amplitude require more time (maximum of 5,000 years). Therefore, the resulting bed level after 5,000 years is used in the remainder of the results. After describing the effects of tides and convergence length on the equilibrium bed profiles, we will discuss the hydrodynamic conditions corresponding to typical bed-level profiles.

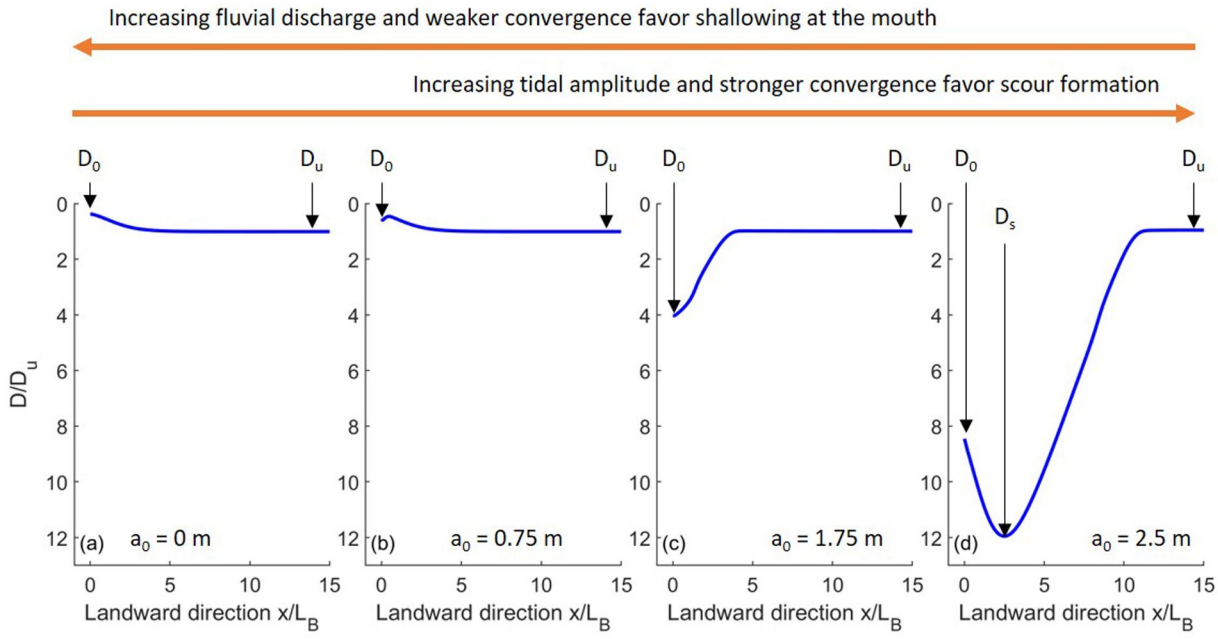

Figure 5. Four typical depth profiles that result from the model runs. The depth (D) is normalized by the upstream river depth (D_u). The mouth depth is indicated by D_0 and the maximum depth along the simulated domain is denoted by D_s. (a) Characteristic profile for a model without tides. (b) Characteristic profile for a small tidal amplitude. (c) Characteristic profile for an intermediate tidal forcing. (d) Characteristic scour profile due to a relatively strong tidal forcing.

3.1. Effects of Tides and Convergence Length on Equilibrium Bed Profiles

Results show that bed levels developed in a similar way for all systems when forced by a progressively increasing tidal amplitude (Figure 5). First, consider a reference simulation in which tides are absent. Without tides, the elevation of the resulting bottom profile increases in seaward direction (Profile A) for a diverging channel (Figure 5a). The shallowing relates to channel widening, flow expansion, and the consequent drop in riverine velocity. Even for low tidal amplitudes (e.g., <0.75 m), the tidal flow lacks the strength to enhance the sediment carrying capacity. By increasing the tidal amplitude further, ebb velocities increase more than flood velocities due to nonlinearities (Equation 5), thus favoring export of sediments to the sea and channel mouth deepening (Bolla Pittaluga et al., 2015). This results in Profile B, where the shallowest section is found within the estuary (Figure 5b). When the tidal amplitude is increased even further, a seaward deepening in the bed profile appears (Profile C). The maximum depth occurs near the mouth (Figure 5c). At even higher amplitudes, the bed level deepens further and a depression establishes landward of the mouth (Figure 5d, Profile D). The transition in depth profiles holds for the full set of scenarios (i.e., for a small, medium, and large estuary (Table 1), in which the tidal range was systematically varied (Figure 6).

The fluvial discharge was varied among the three sets of model runs (Figure 6). A different discharge value also implies a different sediment supply (Equation 12), convergence length (Equations 7 and 8), and riverine bed slope at equilibrium for the three sets of model runs. With a fourfold increase of discharge (e.g., Figure 6c vs. Figure 6a), the sediment supply increased by a factor of about 2.3, which proceeds from Equation 49 in Wilkerson and Parker (2011). While this may be counter-intuitive, an increasing river discharge results in a smaller equilibrium slope, smaller riverine flow velocities, and decreased sediment transport capacity. The lower slope and higher river discharge favor ebb dominance much more than a factor four. This explains why larger tidal amplitudes increasingly promote scours in the model setups with higher discharge (Figure 6c) versus the model setups with lower discharge (Figure 6a). In absence of fluvial discharge and fluvial sediment supply, such as in a tidal channel (Lanzoni & Seminara, 2002), we expect profiles C or D to form (Figures 5c and 5d). Which of the two profiles develops depends on the degree of convergence relative to the tidal amplitude.

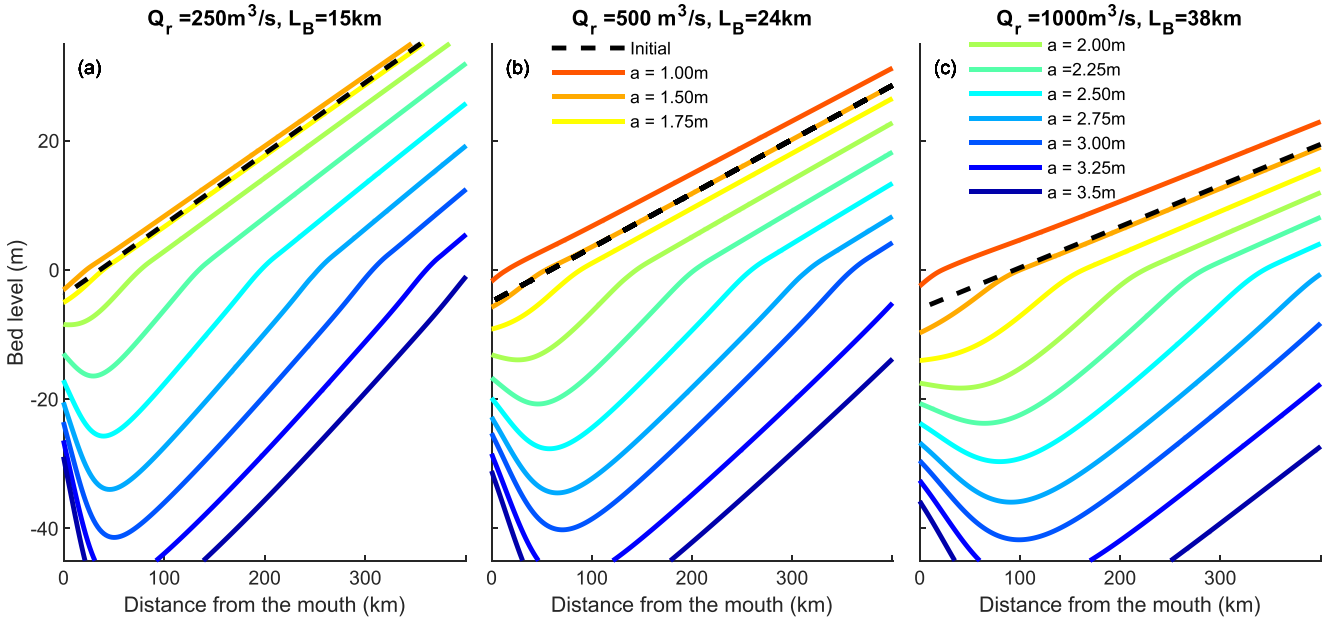

Figure 6. Resulting bed levels in estuaries of three different sizes for varying tidal amplitude after 5,000 years of simulation time. Channel dimensions increase from left to right. Tidal amplitude was varied within each plot according to the legend. Only the most seaward 400 km are shown. The model domain length was 800 km. (a) An estuary with a discharge of 250 m^3/s and a convergence length of 15 km. Note that the model result for a tidal amplitude of 1.0 m was left out for the smallest system (left), because those conditions led to rapid sedimentation at the mouth, which closed off the mouth from the sea. In that case, tides lacked sufficient strength to export the sediment from the mouth. (b) An estuary with a discharge of 500 m^3/s and a convergence length of 24 km. (c) An estuary with a discharge of 1,000 m^3/s and a convergence length of 38 km.

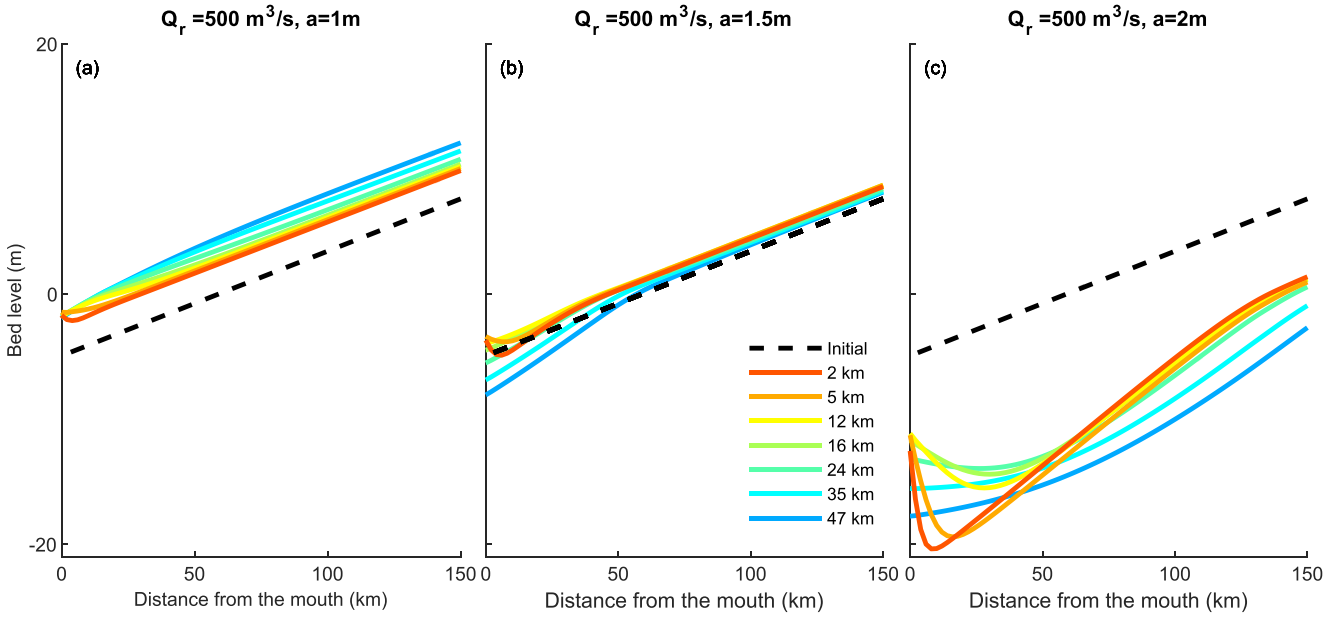

Figure 7. Resulting bed levels in estuaries of three different sizes for varying convergence lengths after 5,000 years of simulation time. Channel dimensions increase from left to right. Convergence length was varied within each plot according to the legend. Only the most seaward 150 km are shown. The model domain length was 800 km. (a) An estuary with a discharge of 500 m^3/s and a tidal amplitude of 1 m. (b) An estuary with a discharge of 500 m^3/s and a tidal amplitude of 1.5 m. (c) An estuary with a discharge of 500 m^3/s and a tidal amplitude of 2 m.

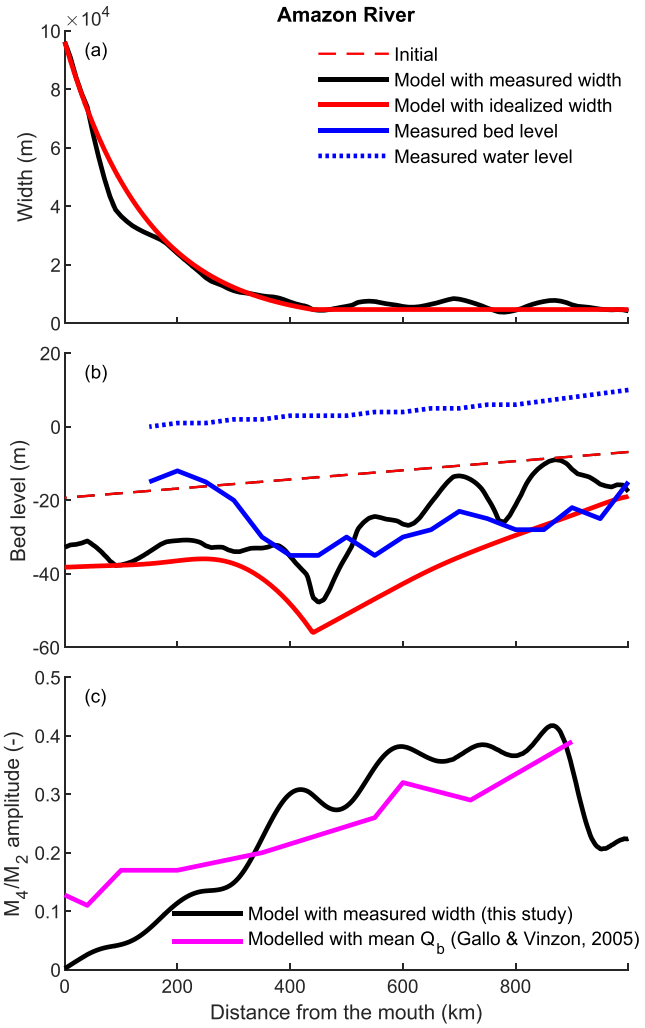

Figure 8. Model simulations for the Amazon River. (a) Along-channel width profiles used as input for the model. (b) Resulting bed-level profiles after 5,000 years of model time. Blue lines indicate an approximation of measured bed levels and water levels from Gallo and Vinzon (2005). The measured bed-level profile was smoothed, because spatial variation in measured bed levels can be ±10–15 m within a few kilometers for the Amazon River. (c) Comparison of M4/M2 tidal amplitudes with model result from Gallo and Vinzon (2005).

Convergence length modulates the degree of funneling of the tide and therefore affects the location, depth, and length of the scour (Figure 7). A short convergence length means a strong gradient in width, which creates strong gradients in sediment transport. Sudden widening at the mouth leads to deposition (or less erosion) and therefore creates a local minimum in the bed-level profile, which creates a local maximum just landward of the mouth. This is most clear in the scenarios with a tidal amplitude of 1.5–2 m and discharge of 500 m^3/s (Figures 7b and 7c). A long convergence length means a mild gradient in sediment transport, which does not create a minimum in the bed-level profile. In that case, the ebb dominance that promotes export (tidal flushing) has a stronger effect than the mechanism that causes sediment deposition at the mouth.

All simulations resulted in very similar profiles, in which differences could mainly be attributed to the tidal amplitude at the mouth, river discharge, sediment supply, and convergence length. The sensitivities to different choices in model set-up are shown in Figure S1. Here we summarize the main outcomes. Smaller sediment supply typically results in a more profound scouring profile (Figure S1a) and the same holds for increasing the discharge while maintaining planform and sediment supply (Figure S1b). Increasing the grain size reduces scouring behavior (Figures S1c and S1d). The friction coefficient has a limited effect on the scour profile (Figure S1e). Lower friction deepens the bed and moves the deepest point slightly landward.

3.2. Potential for Scour in the Amazon River

The idealized model projects the tidal dynamics and large-scale channel bed scour observed in the Amazon River (Figure 8). The bed scour is roughly consistent with bed profile measurements. Maximum channel depth is reached at the point where the converging channel transitions into a channel with a more constant width, for example, at $x = 550$ km. The along-channel bed-level variations are larger when measured width is used, as opposed to an idealized width profile. In the latter case, the topographic forcing of the flow is superimposed on the tide-induced scour effects. Channel widening locally leads to shallower depths, while channel narrowing corresponds with localized scours. Wave distortion increases in landward direction and peaks just before the tidal limit as illustrated by the $M4/M2$ tidal amplitude (Figure 8c).

3.3. Hydrodynamic Conditions That Cause Scour

In all simulations with significant tidal motion we found that, under conditions of morphodynamic equilibrium, the tidal range was fairly constant along the most seaward part of the estuary and then rapidly dampened toward the tidal limit (Figures 9h and 9i). The tidal velocity amplified in the cases for which a scour profile had developed (Figures 9e and 9f) with a peak slightly landward of the maximum depth. Only for estuaries with a small tidal range (e.g., $a_0/D_0 < 1/4$), both the mean current and tidal amplitude rapidly decreased in the estuary mouth region (Figures 9d and 9g). The scour is located along the fluvial-tidal transition zone and the location corresponds to the peak in specific tidal discharge (Figure 9i), defined as the peak discharge per unit width. The specific discharge increases with increasing tidal amplitude (Figures 9g–9i). At the same time, the region of tidal influence extends with increasing tidal amplitude.

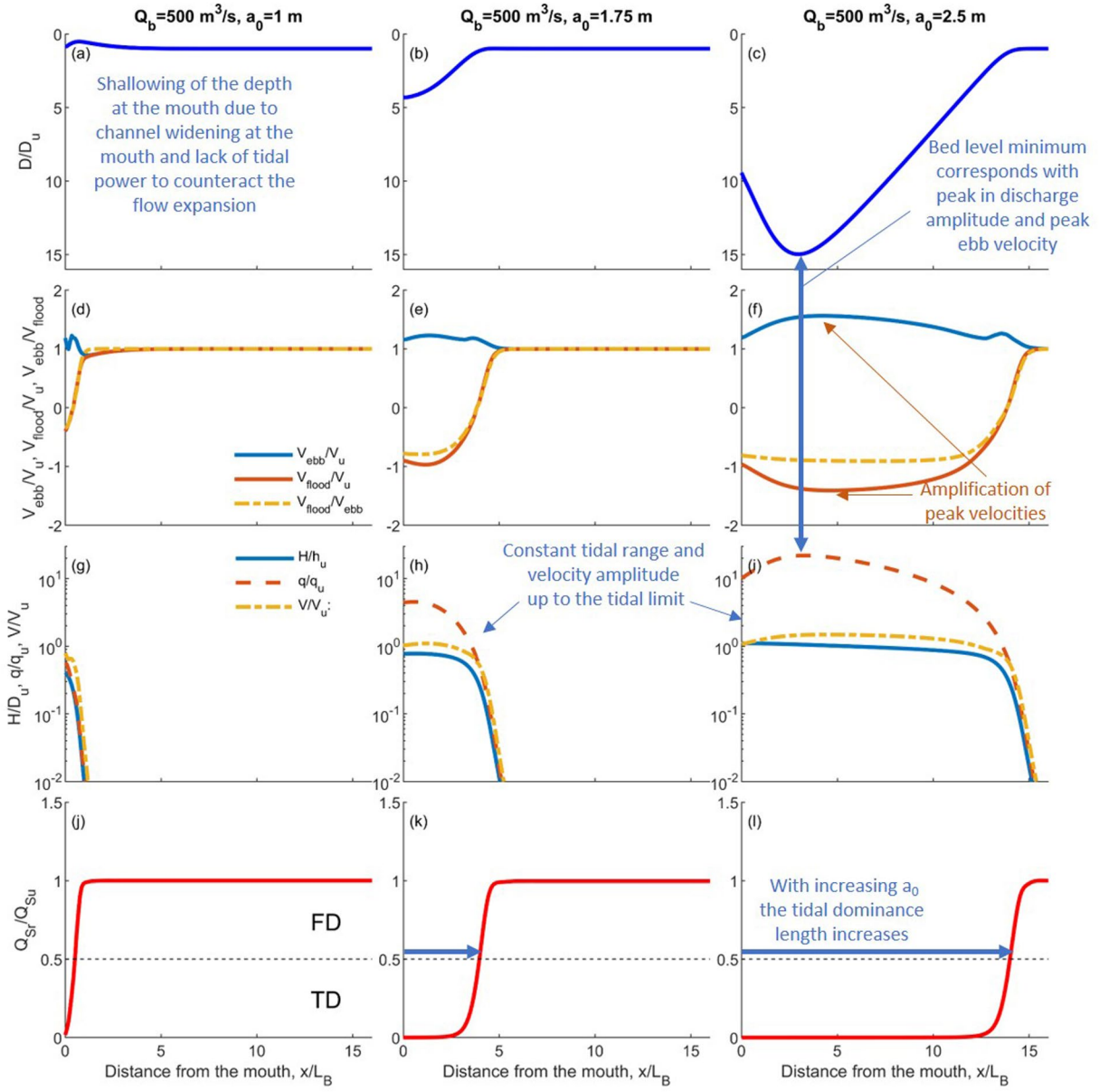

Figure 9. For three selected scenarios in equilibrium (see titles above the plot) with varying degrees of scour, the characteristics of tidal dominance, asymmetry, and sediment transport are shown. In all cases, the distance from the mouth normalized by the convergence length is on the horizontal axes. From top to bottom, the panels show the following on the vertical axes: (a–c) Tidally averaged water depth normalized by the water depth at the upstream boundary; (d–f) Ratios between peak ebb velocity (V_{ebb}), peak flood velocity (V_{flood}), and upstream flow velocity (V_u); (g–i) Amplitudes of water level, specific tidal discharge, and velocity divided by their upstream magnitudes. The amplitudes were computed as the maximum value of the variable minus the minimum divided by 2. (j–l) Sediment load transported by the residual current (Q_{Sr}) divided by the sediment input at the upstream boundary (Q_{Su}). FD stands for fluvial dominance and TD stands for tidal dominance. The point where this line crosses 0.5 is defined as the tidal dominance length (ℓ).

Tidal amplification of the horizontal tide through funneling of tidal energy in the converging region of the estuary can be regarded as the primary cause of scour formation (Figures 9 and 10). Figure 10 shows the decomposition of flow velocity along the estuary. The amplification of the carrier wave increases with an increase of the tidal amplitude at the mouth (Figure 10a).

Most noticeable from the velocity decomposition (Figure 10) is that the hydrodynamics remains very similar among model runs, while the resulting equilibrium bed profiles differ significantly, ranging from convex to concave and scouring. For all runs, maximum wave distortion (largest values of U_4/U_2) is reached near

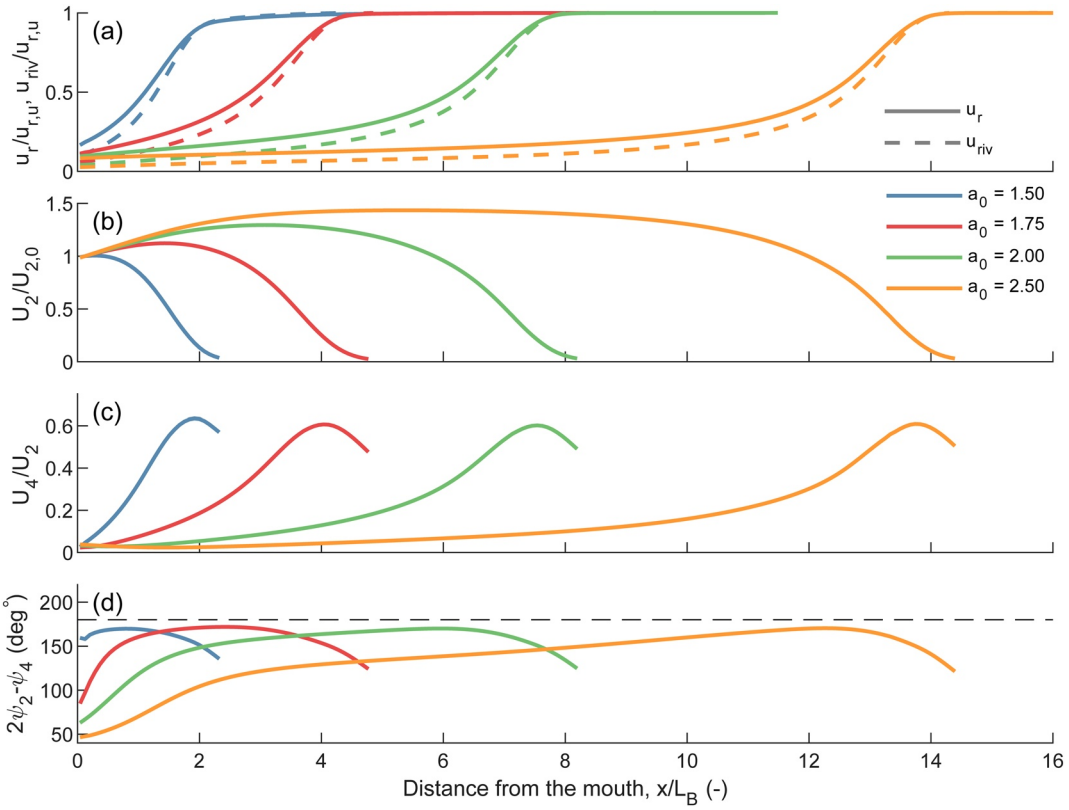

Figure 10. For four selected scenarios in equilibrium with varying degree of scour, the decomposition of flow velocity along the estuary is shown. (a) Residual current (u_r) and river induced current (u_{riv}) normalized by the residual current at the upstream boundary ($u_{r,u}$). The difference between u_r and u_{riv} is the Stokes drift. (b) Velocity amplitude of the semi diurnal (M_2) tide normalized by the amplitude at the mouth. (c) The ratio between the velocity amplitude of the semi-diurnal (M_2) and the quarter-diurnal (M_4) tide. (d) Phase difference between the semi- and quarter-diurnal tide.

the tidal limit, just before energy dissipation exceeds transfer of energy from the carrier wave to the shallow water tides (Figure 10c). A larger tidal amplitude ($a_0 > 1.75$) resulted in a deeper concave bed profile, which limits tidal distortion in the region where the estuary converges (e.g., $x/L_B < 5$). Similarly, when a scour forms, wave distortion is locally reduced at the scour. All runs resulted in flood dominant tidal asymmetry (Figure 10d), as expected for systems that lack intertidal areas (Friedrichs, 2010; Wang et al., 2002). Phase differences were smaller for deeper systems, especially near the mouth, and all systems reach maximum asymmetry near the tidal limit (Figure 10d).

Generally, the residual current weakens toward the estuary mouth (Figure 10a). This reduction is caused by an increasing cross-sectional area as a result of channel deepening and widening of the banks. The Stokes drift contributes significantly to the residual current ($u_{Stokes} = u_r - u_{riv}$) in the tide-dominated region. The Stokes drift increased in the upstream direction, but peaks downstream of the location with maximum wave distortion. It was found that the strength of the Stokes drift relative to the upstream river current (u_{riv}) was slightly weaker for systems with a larger tidal amplitude. This implies that in systems with a smaller tidal amplitude, the extent of the tidally dominated region reduces, because of the stronger contribution of the Stokes drift.

Overall, from the velocity decomposition it can be concluded that amplification of the tide due to funneling is the main hydrodynamic property impacted by the occurrence of a scour profile. Large-scale scours are caused by net sediment transport gradients, which result from the balance between residual current, the interaction between residual current and tides, and by tide asymmetry, which are discussed next.

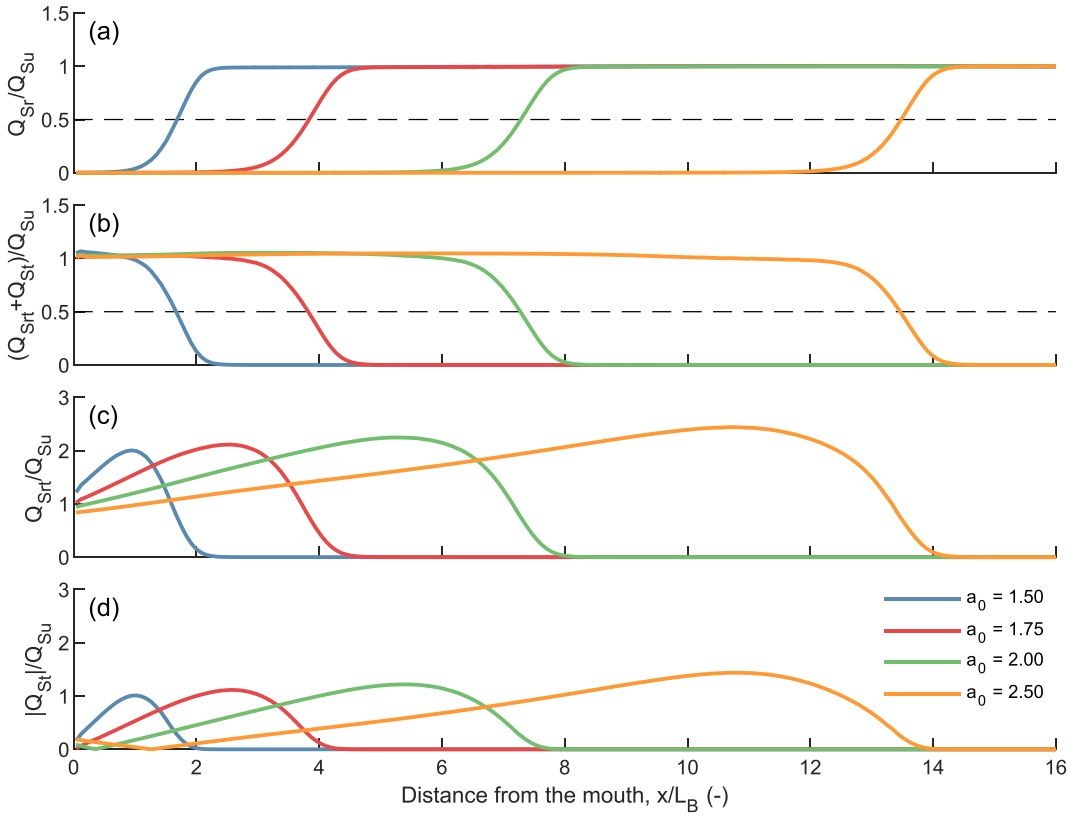

Figure 11. For four selected scenarios in equilibrium with varying degrees of scour, the decomposition of tidal residual sediment transport along the estuary is shown. (a) The sediment load transported by the residual current (Q_{Sr}) divided by the sediment input at the upstream boundary (Q_{Su}). (b) The sum of the sediment load transported by the interaction of the residual current and tidal current (Q_{Srt}) and the sediment transported by tidally induced asymmetry (Q_{St}) divided by the sediment input at the upstream boundary (Q_{Su}). (c) The sediment load transported by the interaction of the residual current and tidal current (Q_{Srt}) divided by the sediment input at the upstream boundary (Q_{Su}). (d) The sediment transported by tidally induced asymmetry (Q_{St}) divided by the sediment input at the upstream boundary (Q_{Su}).

3.4. Residual Sediment Transport

Figure 11 presents the residual sediment transport decomposition. Upstream of the tidal limit, sediment transport is solely determined by the river discharge (Q_{Sr}) (Figure 11a). Toward the mouth, the residual sediment transport reduces to zero and the sediment balance is solely determined by the river-tide interaction (Q_{Srt}) and tide-induced asymmetry (Q_{St}) terms (Figures 11b and 11c). For smaller tidal amplitudes (e.g., $a_0 = 1.5$ m and $a_0 = 1.75$ m), sediment transport within the converging region of the estuary (i.e., for $x/L_B < 5$) is still partly determined by the residual sediment transport, explaining the shallowing of the bed between the fluvial and tidal dominated region (e.g., in Figures 5a and 5b).

In the tide-dominated region, a constant sediment transport is achieved by an interplay between the Q_{Srt} and Q_{St} terms (Figure 11b–11d). Both terms develop in a similar way along the estuary but with an opposite sign. The terms peak downstream of the tidal to fluvial transition. Here, the residual and tidal current are both still strong enough to achieve a maximum in Q_{Srt}. Similarly, the peak in Q_{St} is the result of the most favorable balance between wave distortion and energy dissipation.

One specific distinct feature of a scour profile, which allows for a constant residual sediment transport, is the development of the Q_{St} term. For convex bed profiles, Q_{St} progressively increases as the mean depth decreases and the wave becomes more distorted. In the case of a concave bed profile, the upstream directed Q_{St} terms show a local minimum near the deepest section (Figure 11d, $x/L_B < 2$). This minimum is caused by energy dissipation that exceeds transfer toward the shallow water tides. The weaker Q_{St} term enables the river-tide interaction to provide constant sediment transport trough the deepest section.

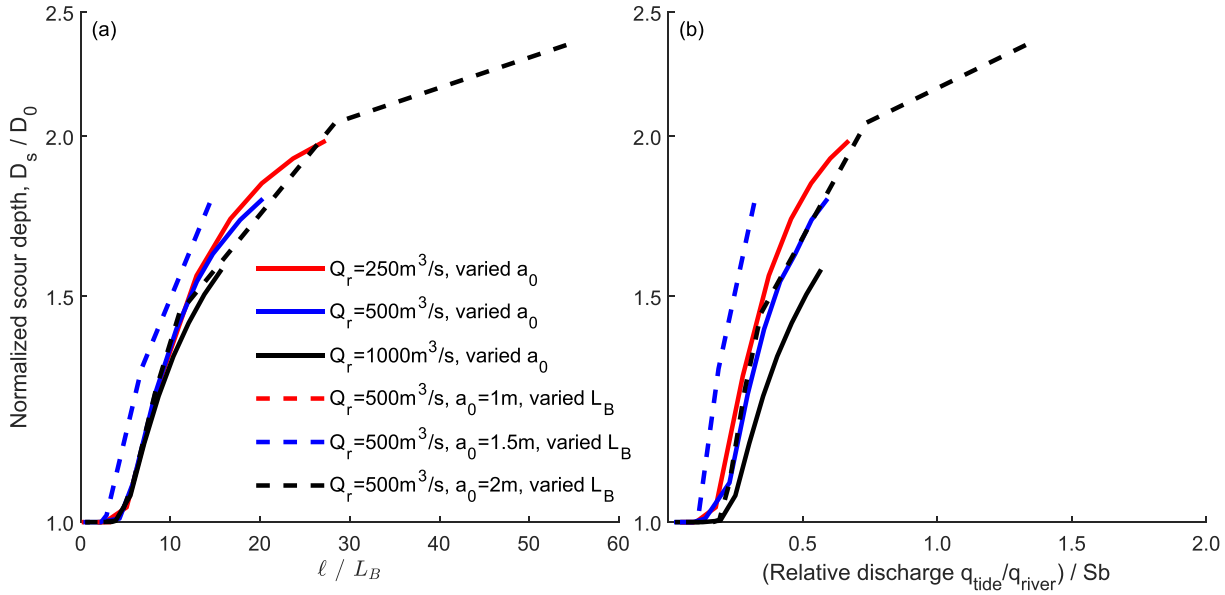

Figure 12. Predictive relations for the occurrence of scours in estuaries. In all cases, the predictor is plotted against the normalized scour depth (i.e., scour depth divided by mouth depth, D_s/D_0). Each line corresponds to a set of scenarios shown in the individual panels in Figures 6 and 7. The following predictors are shown: (a) Tidal dominance length (ℓ) normalized by the convergence length. Tidal dominance length is the distance over which the sediment transport is tide-dominated (see Figures 9j, 9k, and 9l); (b) Ratio between the specific peak tidal discharge at the mouth and the specific river discharge at the landward boundary divided by the shape factor (i.e., convergence length divided by mouth width minus river width $S_B = L_B/(B_0 - B_u)$). The vertical axis is logarithmic to stretch the transitional zone from no scour to scour. Models with a discharge of 500 m^3/s, tidal amplitude of 1 m, and varied convergence (dashed red line) did not result in scouring profiles because tidal influence was too small. This explains why the resulting line plots on top of the leftmost part of the *x*-axis.

3.5. Predictive Relation for the Occurrence of Scour

From Figure 9j, 9k and 9l) it can be observed that scour occurrence is accompanied by an increase in the tidal dominance length (ℓ) relative to the convergence length. Figure 12a reports the normalized tidal dominance length plotted against the normalized scour depth (D_s/D_0). The results indicate a threshold above which scour occurs: $\ell/L_B > 5$, or in other words, the tidal dominance length has to exceed the convergence length by a factor 5 before scour occurs. Only in that case, tidal dominance extends sufficiently beyond the point where channel convergence ceases, resulting in a peak in specific discharge just seaward of that point (Figure 9i). An increasing tidal dominance is accompanied by an increasing flood volume entering the estuary. The convergence length represents the extent to which this volume is funneled into the estuary.

A predictor based on tidal dominance length (ℓ) may be difficult to apply in the absence of any measurements or model results, because ℓ is not a priori known. Therefore, we also develop a predictive relation that captures the same essence, but that is easier to apply. Because the resulting bottom and depth profiles essentially depend on the relative strength of the river current and the amplitude of tidal velocity, we compute the ratio between the specific tidal discharge at the mouth and the specific river discharge at the landward boundary ($q_{\text{tide}}/q_{\text{river}}$) and divide this by the shape factor (S_B).

Figure 12b shows the resulting relation between normalized scour depth and relative strength of tides. Scours develop for values of $\Psi = (q_{\text{tide}}/q_{\text{river}})/S_B$ higher than 0.3. Above this ratio, tidal dominance extends beyond the point where channel convergence ceases, resulting in a peak in specific discharge just seaward of that point (Figure 9i). Increasing tidal discharge while maintaining the same estuary shape would therefore result in increasing chances to form scour. When fluvial and tidal discharges are unknown, fluvial discharge can be estimated from river width and tidal discharge can be estimated from multiplying the estuary surface area by the tidal range (Leuven, de Haas, et al., 2018; Nienhuis et al., 2018).

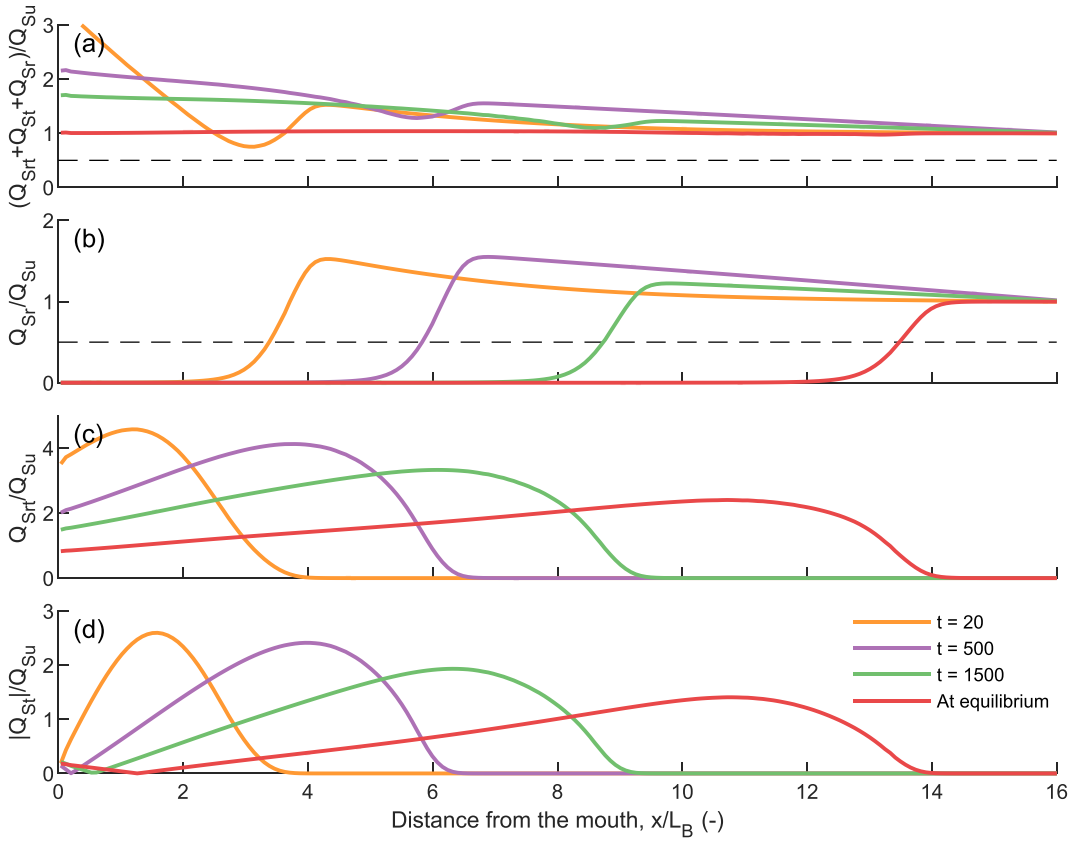

Figure 13. For one selected run (Q_b = 500 m^3/s and a_0 = 2.5 m) the decomposition of tidal residual sediment transport along the estuary is shown over time. (a) The sum of the sediment load transported by the interaction of the residual current and tidal current (Q_{Srt}) and the sediment transported by tidally induced asymmetry (Q_{St}) and the sediment load transported by the residual current (Q_{Sr}) divided by the sediment input at the upstream boundary (Q_{Su}). (b) The sediment load transported by the residual current (Q_{Sr}) divided by the sediment input at the upstream boundary (Q_{Su}). (c) The sediment load transported by the interaction of the residual current and tidal current (Q_{Srt}) divided by the sediment input at the upstream boundary (Q_{Su}). (d) The sediment transported by tidally induced asymmetry (Q_{St}) divided by the sediment input at the upstream boundary (Q_{Su}).

4. Discussion

In summary, the key controlling factors for the occurrence of tide-induced large-scale scours were found to be: tidal amplitude, convergence length, fluvial discharge, and the associated sediment supply. Decreasing sediment supply, decreasing fluvial discharge, increasing tidal amplitude, and decreasing convergence length (i.e., stronger convergence) all favor the formation of a large-scale scour.

4.1. Scour Mechanisms and Relation of Scour With Mouth Bar Morphology

Scour profiles form when an estuary is subject to large tidal amplitudes and when it has a plan-view geometry characterized by strong channel convergence. Independent of the initial conditions, the same equilibrium will be reached (Canestrelli, Lanzoni, & Fagherazzi, 2014). As an example, we reason from a bed profile that is initially monotonically (and linearly) decreasing seaward and that is more shallow than the equilibrium profile. In that case, in the seaward reach there is an initial seaward sediment transport due to the river-tide interaction (caused by an M_2 tide with a residual current) which is much larger than the asymmetry induced landward sediment transport (Figures 13c and 13d). The net seaward transport is larger than the upstream sediment input and this results in channel deepening, which starts at the estuary mouth (Figure 4a). Channel deepening causes a decrease in energy dissipation by bottom friction, thus allowing the tidal wave to propagate even further upstream (Figures 4 and 13). As a consequence, there is a further

increase in seaward transport due to river-tide interaction, which leads to deepening of the bed profile and increasing of the tidal intrusion length. Note that in the region where the width of the estuary approaches its upstream channel width, the strength of the residual current rapidly increases (Figure 13b). This region shows rapid deepening of the bed profile when the tidal motion starts to dominate the local sediment balance, because a combination of tidal influence with a relatively strong residual current creates a strong river-tide interaction. The resulting sediment transport is directed seaward (Figure 13a). This positive-feedback between tidal amplification and scour cannot continue infinitely, and an equilibrium will be reached when the bed profile is characterized by a large-scale scour (Figures 4a and 13a). In fact, since the residual freshwater discharge is constant along the estuary, for a scouring profile the increase in depth leads to a drop in river induced flow magnitude. As a consequence, the river-tide interaction contribution to sediment transport is reduced. Scouring proceeds until the net seaward transport balances the upstream sediment transport. This leads to an equilibrium configuration characterized by a zero gradient in net transport along the estuary (Figure 13a).

The bed profiles that results from the tide-induced scour mechanism (Figure 5) can be interpreted in the context of morphological observations of mouth bars (Canestrelli, Nardin, et al., 2014; Edmonds & Slingerland, 2007). In the case of a rapid widening at the mouth (e.g., a strong width convergence and a lack of sufficient tidal strength), a mouth bar is formed. This translates to a bed profile with a minimum elevation followed by a sudden increase in bed level at the seaward tip of the estuary (Figures 5 and 7c). With increasing tidal influence or decreasing width convergence, the shallow zone at the mouth becomes longer and the bed level minimum becomes less pronounced (Figure 7c). This mouth morphology consisting of elongated mouth bars is observed in natural systems, such as in the Fly River delta. For even stronger tides or lower width convergence, the mouth bars disappear completely and the mouth becomes the deepest point. This relation between width-averaged bed level and mouth bar morphology needs further investigation, but if the correlation indeed holds, mouth bar morphology may reveal information about potential scouring behavior of the channel bed.

4.2. Comparison With Earlier Studies

While the model set-up of Bolla Pittaluga et al. (2015) was similar to our set-up, their results surprisingly lacked any bed profiles with scours. Most comparable with our study are the results presented in Figure 14c in Bolla Pittaluga et al. (2015), because they are based on scenarios with tides in a convergent channel. The main difference here is that their river discharge (1,000 m^3/s) and sediment supply (0.355 m^3/s) were remarkably large, considering a river width of 182 m. Indeed, this river width corresponds to a bankfull discharge of 1,000 m^3/s, according to hydraulic geometry relations (Equation 7). Estimating the relative dominance of river discharge and tides result in values of $(q_{tide}/q_{river})/S_B$ between 0.2−0.25 for relatively large tidal amplitude, that is, between 3.0 and 4.0 m. It is consistent with our predictor, that in this case, no scour is formed (Figure 12b).

Moreover, the sediment supply in Bolla Pittaluga et al. (2015) was about twice what we would predict for the same discharge (e.g., 0,1733 m^3/s with Equation 12 with Chézy = 55) and about 10 times larger than our estimate for yearly average discharge. Relating sediment supply to bankfull conditions without implementation of an intermittency factor (Paola et al., 1992) results in a overestimation of the sediment delivery to the estuary over centuries, which explains the absence of scouring profiles in their results (Figures S1a and S1b).

In scenarios of prismatic channels with tides, Bolla Pittaluga et al. (2015) observed a deepening of the bed profile toward the mouth. Because channel width remains constant, the added effect of tides is an increased tidal prism and therefore higher peak velocities during ebb. The ratio between increase in tidal prism (TP) and increase in width in seaward direction (dTP/dW) determines the resulting bed profile. These results are consistent with our predictive relation (Figure 12) in the sense that a prismatic channel can be seen as a channel with almost infinite convergence length. In that case, our metric indeed predicts the absence of a scour.

For the Fly River, Canestrelli, Lanzoni, and Fagherazzi (2014) obtained a scour at about 250–300 km from the mouth (see Figure 7 in the original paper). This bed-level profile was obtained by prescribing bankfull discharge, which in the case of the Fly River is very similar to the mean annual discharge (Dietrich et al., 1999; Wolanski et al., 1997). Estimating the relative dominance of river discharge and tides result in an $(q_{tide}/q_{river})/S_B$ that is approximately 1, which means that the resulting scour is consistent with our predictor (Figure 12b).

4.3. Implications

Large-scale scours might occur in many estuaries. Our model results show scours for river discharges from 250–1,000 m^3/s and tidal amplitudes between 1–3.5 m. Beyond our model results, we checked in the data set of Nienhuis et al. (2020) which coastal rivers might have large-scale scours. The database consists of wave-dominated deltas, river-dominated deltas, and alluvial estuaries. We found that 568 out of 10,848 deltas have $(q_{tide}/q_{river})/S_B$ exceeding 0.3, including the Amazon (Q_b = 169,000 m^3/s, a_0 = 2.5 m). Of those deltas, discharge spans 1–169,000 m^3/s and tidal amplitudes vary from 0.8 m to >5 m, indicating broad, global occurrence. Direct observation of tide-induced scours may often be complicated by human controls on channel geometries (Hoitink et al., 2020), and geological constraints that obscure the scour effect.

The tide-induced scour mechanism has implications for the response of estuaries to sea-level rise and human influence. Sea-level rise increases water depth and reduces friction, which will increase tidal dominance over fluvial dominance (Boelens et al., 2018; Du et al., 2018; Friedrichs & Aubrey, 1988; Savenije, 2006; Silvestri et al., 2018). Moreover, tidal amplitudes at the mouth may increase (or decrease) due to shifting amphidromic points (Idier et al., 2017; Pickering et al., 2017), which effectively increases (or decreases) tidal dominance as well. Lastly, construction of flood-control dams globally reduces fluvial discharge and sediment supply to river mouths (Dunn et al., 2019; Walling & Fang, 2003; Yang et al., 2005), which again favors the formation of large-scale scours. A similar reasoning applies to changes in land-use or other climate change scenarios.

All factors increasing tidal dominance, decreasing fluvial dominance or fluvial sediment supply contribute to an increased potential for scour occurrence and increased scour depth. By changing those boundary conditions, either the channel width or the depth has to adjust. In case of bank protection (Hoitink et al., 2017; Temmerman & Kirwan, 2015), it must be the latter. If large-scale channel bed scour develops, banks are steepened, thus threatening channel bank stability. Providing more space for river mouths needs further exploration, as potential adaptation strategy (Haasnoot et al., 2013; Kwadijk et al., 2010; Leuven et al., 2019; Schuerch et al., 2018) to cope with unwanted effects of future changes in boundary conditions.

5. Conclusions

We have found a predictor for scour occurrence in estuaries that depends on two dimensionless parameters: (a) the planform shape factor (S_B), which is a measure of channel width convergence, and (b) the ratio between the specific peak tidal discharge at the mouth versus the specific river discharge at the landward boundary (q_{tide}/q_{river}). This can be expressed using a predictor of the form $\Psi = (q_{tide}/q_{river})/S_B$. For values of Ψ exceeding 0.3, large-scale scours develop. The conditions that may cause scours were found to occur globally across a range of fluvial and tidal scales. The results allow to predict the potential of channel bed scour in estuaries under future changes in boundary conditions.

To arrive at this predictor, we systematically investigated the effect of tidal dominance on the equilibrium channel bed with a 1D-morphodynamic model. Large tidal amplitudes promote the formation of a large-scale scour in the bed profile. Scours form when tidal velocities are further amplified in the width-converging region of the estuary. When the tidal discharge is relatively high compared to the fluvial discharge, and the channel width converges rapidly, a bed-level profile characterized by a monotonically decreasing bed elevation in the seaward direction is unstable. For such a linear bed profile, the river-tide interaction contribution to the residual sediment transport is large in the funneling region, and establishes a net seaward transport larger than the rate of upstream sediment input. A morphodynamic equilibrium is only possible with a scoured profile, for which the drop in river induced flow strength reduces river-tide interaction,

resulting in constant residual sediment transport along the bed profile. This leads to an equilibrium configuration characterized by zero gradients in net transport along the estuary.

Data Availability Statement

The numerical model set-up, model results, data used, and code to reproduce the figures are all available from Zenodo (https://doi.org/10.5281/zenodo.4593450). Data used to initialize models for the Amazon River are listed in the references.

Acknowledgments
This research was supported by the Dutch Technology Foundation TTW (grant Vici 17062 to AJFH), which is part of the Netherlands Organisation for Scientific Research (NWO), and is partly funded by the Ministry of Economic Affairs. J. H. Nienhuis acknowledges support from NWO Veni 192.123. This work was part of the MSc research project of DvK. The authors declare that they have no conflict of interest. Reviews by three anonymous reviewers, and steer by the Editor and Associate Editor helped to improve the manuscript.

References

Ashworth, P. J., Best, J. L., & Parsons, D. R. (2015). Fluvial-tidal sedimentology (Vol. 68). Elsevier.
Boelens, T., Schuttelaars, H., Schramkowski, G., & de Mulder, T. (2018). The effect of geometry and tidal forcing on hydrodynamics and net sediment transport in semi-enclosed tidal basins. *Ocean Dynamics*, *68*(10), 1285–1309. https://doi.org/10.1007/s10236-018-1198-9
Bolla Pittaluga, M., Tambroni, N., Canestrelli, A., Slingerland, R., Lanzoni, S., & Seminara, G. (2015). Where river and tide meet: The morphodynamic equilibrium of alluvial estuaries. *Journal of Geophysical Research: Earth Surface*, *120*(1), 75–94. https://doi.org/10.1002/2014jf003233
Bouma, H, de Jong, D. J, Twisk, F., & Wolfstein, K. (2005). *A Dutch ecotope system for coastal waters (zes. 1), to map the potential occurence of ecological communities in Dutch coastal and transitional waters* (Technical Report RIKZ/2005.024). Rijkswaterstaat.
Braat, L., van Kessel, T., Leuven, J. R. F. W., & Kleinhans, M. G. (2017). Effects of mud supply on large-scale estuary morphology and development over centuries to millennia. *Earth Surface Dynamics*, *5*(4), 617–652. https://doi.org/10.5194/esurf-5-617-2017
Buschman, F., Hoitink, A., Van Der Vegt, M., & Hoekstra, P. (2010). Subtidal flow division at a shallow tidal junction. *Water Resources Research*, *46*(12). https://doi.org/10.1029/2010wr009266
Canestrelli, A., Lanzoni, S., & Fagherazzi, S. (2014). One-dimensional numerical modeling of the long-term morphodynamic evolution of a tidally-dominated estuary: The lower Fly River (Papua New Guinea). *Sedimentary Geology*, *301*, 107–119. https://doi.org/10.1016/j.sedgeo.2013.06.009
Canestrelli, A., Nardin, W., Edmonds, D., Fagherazzi, S., & Slingerland, R. (2014). Importance of frictional effects and jet instability on the morphodynamics of river mouth bars and levees. *Journal of Geophysical Research: Oceans*, *119*(1), 509–522. https://doi.org/10.1002/2013jc009312
D'Alpaos, A., Ghinassi, M., Finotello, A., Brivio, L., Bellucci, L. G., & Marani, M. (2017). Tidal meander migration and dynamics: A case study from the Venice lagoon. *Marine and Petroleum Geology*, *87*, 80–90. https://doi.org/10.1016/j.marpetgeo.2017.04.012
Dalrymple, R. W., Baker, E. K., Harris, P. T., & Hughes, M. G. (2003). Sedimentology and stratigraphy of a tide-dominated, foreland-basin delta (Fly River, Papua New Guinea). In F. Hasan Sidi, D. Nummedal, P. Imbert, H. Darman, & H. W. Posamentier (Eds.), *Tropical deltas of Southeast Asia—Sedimentology, stratigraphy, and petroleum geology* (pp. 147–173).
Davies, G., & Woodroffe, C. D. (2010). Tidal estuary width convergence: Theory and form in north Australian estuaries. *Earth Surface Processes and Landforms*, *35*(7), 737–749. https://doi.org/10.1002/esp.1864
de Vriend, H. J., Wang, Z. B., Ysebaert, T., Herman, P. M. J., & Ding, P. (2011). Eco-morphological problems in the Yangtze estuary and the Western Scheldt. *Wetlands*, *31*(6), 1033–1042. https://doi.org/10.1007/s13157-011-0239-7
Dietrich, W., Day, G., & Parker, G. (1999). The Fly River, Papua New Guinea: Inferences about river dynamics, floodplain sedimentation and fate of sediment. *Varieties of fluvial form*, 345–376.
Dronkers, J. (2017). Convergence of estuarine channels. *Continental Shelf Research*, *144*, 120–133. https://doi.org/10.1016/j.csr.2017.06.012
Du, J., Shen, J., Zhang, Y. J., Ye, F., Liu, Z., Wang, Z., et al. (2018). Tidal response to sea-level rise in different types of estuaries: The importance of length, bathymetry, and geometry. *Geophysical Research Letters*, *45*(1), 227–235. https://doi.org/10.1002/2017GL075963
Dunn, F. E., Darby, S. E., Nicholls, R. J., Cohen, S., Zarfl, C., & Fekete, B. M. (2019). Projections of declining fluvial sediment delivery to major deltas worldwide in response to climate change and anthropogenic stress. *Environmental Research Letters*, *14*(8), 084034. https://doi.org/10.1088/1748-9326/ab304e
Dunne, K. B., & Jerolmack, D. J. (2020). What sets river width? *Science Advances*, *6*(41), eabc1505. https://doi.org/10.1126/sciadv.abc1505
Edmonds, D. A., Caldwell, R. L., Brondizio, E. S., & Siani, S. M. (2020). Coastal flooding will disproportionately impact people on river deltas. *Nature Communications*, *11*(1), 1–8. https://doi.org/10.1038/s41467-020-18531-4
Edmonds, D. A., & Slingerland, R. (2007). Mechanics of river mouth bar formation: Implications for the morphodynamics of delta distributary networks. *Journal of Geophysical Research*, *112*(F2). https://doi.org/10.1029/2006jf000574
Engelund, F., & Hansen, E. (1967). *A monograph on sediment transport in alluvial streams* (Technical Report). Technical University of Denmark.
Friedrichs, C. T. (2010). *Contemporary issues in estuarine physics* (pp. 27–61). Cambridge University Press.
Friedrichs, C. T., & Aubrey, D. G. (1988). Non-linear tidal distortion in shallow well-mixed estuaries: A synthesis. *Estuarine, Coastal and Shelf Science*, *27*(5), 521–545. https://doi.org/10.1016/0272-7714(88)90082-0
Gallo, M. N., & Vinzon, S. B. (2005). Generation of overtides and compound tides in amazon estuary. *Ocean Dynamics*, *55*(5–6), 441–448. https://doi.org/10.1007/s10236-005-0003-8
Guo, L., van der Wegen, M., Roelvink, D., & He, Q. (2015a). Exploration of the impact of seasonal river discharge variations on long-term estuarine morphodynamic behavior. *Coastal Engineering*, *95*, 105–116. https://doi.org/10.1016/j.coastaleng.2014.10.006
Guo, L., van der Wegen, M., Roelvink, J. A., & He, Q. (2015b). The role of river flow and tidal asymmetry on 1-d estuarine morphodynamics. *Journal of Geophysical Research: Earth Surface*, *119*(11), 2315–2334. https://doi.org/10.1016/j.csr.2015.09.002
Haasnoot, M., Kwakkel, J. H., Walker, W. E., & ter Maat, J. (2013). Dynamic adaptive policy pathways: A method for crafting robust decisions for a deeply uncertain world. *Global Environmental Change*, *23*(2), 485–498. https://doi.org/10.1016/j.gloenvcha.2012.12.006
Hart, B. S. (1995). Chapter 7: Delta front estuaries. In *Delta front estuaries. Geomorphology and sedimentology of estuaries* (pp. 207–226). Elsevier. https://doi.org/10.1016/s0070-4571(05)80027-5
Hey, R. D., & Thorne, C. R. (1986). Stable channels with mobile gravel beds. *Journal of Hydraulic Engineering*, *112*(8), 671–689. https://doi.org/10.1061/(ASCE)0733-942910.1061/(asce)0733-9429(1986)112:8(671)

Hoitink, A. J. F., Nittrouer, J. A., Passalacqua, P., Shaw, J. B., Langendoen, E. J., Huismans, Y., & van Maren, D. S. (2020). Resilience of river deltas in the anthropocene. *Journal of Geophysical Research: Earth Surface*, *125*(3). https://doi.org/10.1029/2019jf005201

Hoitink, A. J. F., Wang, Z. B., Vermeulen, B., Huismans, Y., & Kästner, K. (2017). Tidal controls on river delta morphology. *Nature Geoscience*, *10*(9), 637–645. https://doi.org/10.1038/ngeo3000

Idier, D., Paris, F., Cozannet, G. L., Boulahya, F., & Dumas, F. (2017). Sea-level rise impacts on the tides of the European shelf. *Continental Shelf Research*, *137*, 56–71. https://doi.org/10.1016/j.csr.2017.01.007

Kästner, K., Hoitink, A. J. F., Vermeulen, B., Geertsema, T. J., & Ningsih, N. S. (2017). Distributary channels in the fluvial to tidal transition zone. *Journal of Geophysical Research: Earth Surface*, *122*(3), 696–710. https://doi.org/10.1002/2016jf004075

Kleinhans, M. G., & van den Berg, J. H. (2011). River channel and bar patterns explained and predicted by an empirical and a physics-based method. *Earth Surface Processes and Landforms*, *36*(6), 721–738. https://doi.org/10.1002/esp.2090

Kleinhans, M. G., van der Vegt, M., Leuven, J., Braat, L., Markies, H., Simmelink, A., et al. (2017). Turning the tide: Comparison of tidal flow by periodic sea level fluctuation and by periodic bed tilting in scaled landscape experiments of estuaries. *Earth Surface Dynamics*, *5*(4), 731–756. https://doi.org/10.5194/esurf-2017-1110.5194/esurf-5-731-2017

Kosuth, P., Callède, J., Laraque, A., Filizola, N., Guyot, J. L., Seyler, P., et al. (2009). Sea-tide effects on flows in the lower reaches of the amazon river. *Hydrological Processes*, *23*(22), 3141–3150. https://doi.org/10.1002/hyp.7387

Kwadijk, J. C. J., Haasnoot, M., Mulder, J. P. M., Hoogvliet, M. M. C., Jeuken, A. B. M., van der Krogt, R. A. A., et al. (2010). Using adaptation tipping points to prepare for climate change and sea level rise: A case study in The Netherlands. *WIREs Climate Change*, *1*(5), 729–740. https://doi.org/10.1002/wcc.64

Lamb, M. P., Nittrouer, J. A., Mohrig, D., & Shaw, J. (2012). Backwater and river plume controls on scour upstream of river mouths: Implications for fluvio-deltaic morphodynamics. *Journal of Geophysical Research*, *117*(F1). https://doi.org/10.1029/2011jf002079

Lane, E. W. (1957). *A study of the shape of channels formed by natural streams flowing in erodible material*.

Langbein, W. B. (1963). The hydraulic geometry of a shallow estuary. *International Association of Scientific Hydrology. Bulletin*, *8*(3), 84–94. https://doi.org/10.1080/02626666309493340

Lanzoni, S., & Seminara, G. (2002). Long-term evolution and morphodynamic equilibrium of tidal channels. *Journal of Geophysical Research*, *107*(C1), 1–13. https://doi.org/10.1029/2000JC000468

Latrubesse, E. M., Arima, E. Y., Dunne, T., Park, E., Baker, V. R., d'Horta, F. M., et al. (2017). Damming the rivers of the amazon basin. *Nature*, *546*(7658), 363–369. https://doi.org/10.1038/nature22333

Leopold, L. B., & Maddock, T., Jr. (1953). *The hydraulic geometry of stream channels and some physiographic implications* (Technical Report No. Professional Paper 252). U.S. Geological Survey. https://doi.org/10.3133/pp252

Leuven, J. R. F. W., Braat, L., Dijk, W. M., Haas, T., Onselen, E. P., Ruessink, B. G., & Kleinhans, M. G. (2018). Growing forced bars determine nonideal estuary planform. *Journal of Geophysical Research: Earth Surface*, *123*(11), 2971–2992. https://doi.org/10.1029/2018JF004718

Leuven, J. R. F. W., de Haas, T., Braat, L., & Kleinhans, M. G. (2018). Topographic forcing of tidal sandbar patterns for irregular estuary planforms. *Earth Surface Processes and Landforms*, *43*, 172–186. https://doi.org/10.1002/esp.4166

Leuven, J. R. F. W., Pierik, H. J., Vegt, M. v. d., Bouma, T. J., & Kleinhans, M. G. (2019). Sea-level-rise-induced threats depend on the size of tide-influenced estuaries worldwide. *Nature Climate Change*, *9*(12), 986–992. https://doi.org/10.1038/s41558-019-0608-4

Leuven, J. R. F. W., van Maanen, B., Lexmond, B. R., van der Hoek, B. V., Spruijt, M. J., & Kleinhans, M. G. (2018). Dimensions of fluvial-tidal meanders: Are they disproportionally large? *Geology*, *46*(10), 923–926. https://doi.org/10.1130/G45144.1

Mikhailov, V. (1970). Hydrologic-morphometric characteristics of delta branches. *Stud. Rep. Hydrol*, *9*, 146–158.

Nienhuis, J. H., Ashton, A. D., Edmonds, D. A., Hoitink, A. J. F., Kettner, A. J., Rowland, J. C., & Törnqvist, T. E. (2020). Global-scale human impact on delta morphology has led to net land area gain. *Nature*, *577*(7791), 514–518. https://doi.org/10.1038/s41586-019-1905-9

Nienhuis, J. H., Hoitink, A. J. F., & Törnqvist, T. E. (2018). Future change to tide-influenced deltas. *Geophysical Research Letters*, *45*(8), 3499–3507. https://doi.org/10.1029/2018gl077638

Nordin, C. F., Meade, R. H., Curtis, W. F., Bósio, N. J., & Landim, P. M. B. (1980). Size distribution of amazon river bed sediment. *Nature*, *286*(5768), 52–53. https://doi.org/10.1038/286052a0

Paola, C., Heller, P. L., & Angevine, C. L. (1992). The large-scale dynamics of grain-size variation in alluvial basins, 1: Theory. *Basin Research*, *4*(2), 73–90. https://doi.org/10.1111/j.1365-2117.1992.tb00145.x

Pickering, M. D., Horsburgh, K. J., Blundell, J. R., Hirschi, J. J.-M., Nicholls, R. J., Verlaan, M., & Wells, N. C. (2017). The impact of future sea-level rise on the global tides. *Continental Shelf Research*, *142*, 50–68. https://doi.org/10.1016/j.csr.2017.02.004

Roelvink, J. A. (2006). Coastal morphodynamic evolution techniques. *Coastal Engineering*, *53*(2–3), 277–287. https://doi.org/10.1016/j.coastaleng.2005.10.015

Sassi, M. G., Hoitink, A. J. F., de Brye, B., Vermeulen, B., & Deleersnijder, E. (2011). Tidal impact on the division of river discharge over distributary channels in the mahakam delta. *Ocean Dynamics*, *61*(12), 2211–2228. https://doi.org/10.1007/s10236-011-0473-9

Savenije, H. H. G. (2006). *Salinity and tides in alluvial estuaries*. Elsevier.

Schuerch, M., Spencer, T., Temmerman, S., Kirwan, M. L., Wolff, C., Lincke, D., et al. (2018). Future response of global coastal wetlands to sea-level rise. *Nature*, *561*(7722), 231–234. https://doi.org/10.1038/s41586-018-0476-5

Seminara, G., Lanzoni, S., Tambroni, N., & Toffolon, M. (2010). How long are tidal channels? *Journal of Fluid Mechanics*, *643*, 479–494. https://doi.org/10.1017/s0022112009992308

Silvestri, S., D'Alpaos, A., Nordio, G., & Carniello, L. (2018). Anthropogenic modifications can significantly influence the local mean sea level and affect the survival of salt marshes in shallow tidal systems. *Journal of Geophysical Research: Earth Surface*, *123*(5), 996–1012. https://doi.org/10.1029/2017JF004503

Tambroni, N., Bolla Pittaluga, M., & Seminara, G. (2005). Laboratory observations of the morphodynamic evolution of tidal channels and tidal inlets. *Journal of Geophysical Research*, *110*(F4), 1–23. https://doi.org/10.1029/2004JF000243

Temmerman, S., & Kirwan, M. L. (2015). Building land with a rising sea. *Science*, *349*(6248), 588–589. https://doi.org/10.1126/science.aac8312

Todeschini, I., Toffolon, M., & Tubino, M. (2008). Long-term morphological evolution of funnel-shape tide-dominated estuaries. *Journal of Geophysical Research*, *113*(C5). https://doi.org/10.1029/2007jc004094

Toffolon, M., & Lanzoni, S. (2010). Morphological equilibrium of short channels dissecting the tidal flats of coastal lagoons. *Journal of Geophysical Research*, *115*(F4), 1–15. https://doi.org/10.1029/2010JF001673

Townend, I. (2012). The estimation of estuary dimensions using a simplified form model and the exogenous controls. *Earth Surface Processes and Landforms*, *37*(15), 1573–1583. https://doi.org/10.1002/esp.3256

Venditti, J. G., Domarad, N., Church, M., & Rennie, C. D. (2015). The gravel-sand transition: Sediment dynamics in a diffuse extension. *Journal of Geophysical Research: Earth Surface*, *120*(6), 943–963. https://doi.org/10.1002/2014jf003328

Walling, D. E., & Fang, D. (2003). Recent trends in the suspended sediment loads of the world's rivers. *Global and Planetary Change*, *39*(1–2), 111–126. https://doi.org/10.1016/S0921-8181(03)00020-1

Wang, Z. B., Jeuken, M. C. J. L., Gerritsen, H., de Vriend, H. J., & Kornman, B. A. (2002). Morphology and asymmetry of the vertical tide in the Western Schelde estuary. *Continental Shelf Research*, *22*(17), 2599–2609. https://doi.org/10.1016/s0278-4343(02)00134-6

Wilkerson, G. V., & Parker, G. (2011). Physical basis for quasi-universal relationships describing bankfull hydraulic geometry of sand-bed rivers. *Journal of Hydraulic Engineering*, *137*(7), 739–753. https://doi.org/10.1061/(asce)hy.1943-7900.0000352

Wolanski, E., King, B., & Galloway, D. (1997). Salinity intrusion in the Fly River estuary, Papua New Guinea. *Journal of Coastal Research*, 983–994.

Yang, S. L., Zhang, J., Zhu, J., Smith, J. P., Dai, S. B., Gao, A., & Li, P. (2005). Impact of dams on Yangtze river sediment supply to the sea and delta intertidal wetland response. *Journal of Geophysical Research*, *110*(F3), 1–12. https://doi.org/10.1029/2004JF000271